Acoustic Emission Beamforming for Detection and Localization of Damage

Joshua Callen Rivey

A thesis submitted in partial fulfillment of the
requirements for the degree of

Master of Science

University of Washington

2016

Committee:

Jinkyu Yang, Chair

Marco Salviato

Program Authorized to Offer Degree:
Aeronautics and Astronautics

University of Washington

Abstract

Acoustic Emission Beamforming for Detection and Localization of Damage

Joshua Callen Rivey

Chair of the Supervisory Committee:
Associate Professor Jinkyu Yang
UW Aeronautics and Astronautics

The aerospace industry is a constantly evolving field with corporate manufacturers continually utilizing innovative processes and materials. These materials include advanced metallics and composite systems. The exploration and implementation of new materials and structures has prompted the development of numerous structural health monitoring and nondestructive evaluation techniques for quality assurance purposes and pre- and in-service damage detection. Exploitation of acoustic emission sensors coupled with a beamforming technique provides the potential for creating an effective non-contact and non-invasive monitoring capability for assessing structural integrity. This investigation used an acoustic emission detection device that employs helical arrays of MEMS-based microphones around a high-definition optical camera to provide real-time non-contact monitoring of inspection specimens during testing. The study assessed the feasibility of the sound camera for use in structural health monitoring of composite specimens during tensile testing for detecting onset of damage in addition to nondestructive evaluation of aluminum inspection plates for visualizing stress wave propagation in structures.

During composite material monitoring, the sound camera was able to accurately identify the onset and location of damage resulting from large amplitude acoustic feedback mechanisms such as fiber breakage. Damage resulting from smaller acoustic feedback events such as matrix failure was detected but not localized to the degree of accuracy of larger feedback

events. Findings suggest that beamforming technology can provide effective non-contact and non-invasive inspection of composite materials, characterizing the onset and the location of damage in an efficient manner. With regards to the nondestructive evaluation of metallic plates, this remote sensing system allows us to record wave propagation events in situ via a single-shot measurement. This is a significant improvement over the conventional wave propagation tracking technique based on laser doppler vibrometry that requires synchronization of data acquired from numerous excitations and measurements. The proposed technique can be used to characterize and localize damage by detecting the scattering, attenuation, and reflections of stress waves resulting from damage and defects. These studies lend credence to the potential development of new SHM/NDE techniques based on acoustic emission beamforming for characterizing a wide spectrum of damage modes in next-generation materials and structures without the need for mounted contact sensors.

TABLE OF CONTENTS

LIST OF FIGURES

LIST OF TABLES

GLOSSARY

AE: Acoustic Emissions

CCD: Charge-Coupled Devices

FPGA: Field-Programmable Gate Array

FPS: Frames Per Second

MEMS: Micro-Electric Mechanical System

NDE: Nondestructive Evalution

NDI: Nondestructive Inspection

NDT: Nondestructive Testing

UD: Uni-Directional

ACKNOWLEDGMENTS

I would like to express my sincere gratitude to the University of Washington and the members of the Department of Aeronautics and Astronautics for providing me the opportunity to pursue this esteemed degree. First, I would like to thank Professor Jinkyu Yang, my advisor and committee chair, for his guidance, motivation, and encouragement for the research contained herein. I extend copious amounts of appreciation to Dr. Gil-Yong Lee, Research Associate, for his assistance in this research and for infusing life into this project. Thank you to Youngkey Kim, InKwon Kim, and JunGoo Kang of SM Instruments for allowing us to use their sound camera and for their acoustic expertise and technical assistance that made the sound camera so successful for this research. Thank you to Bill Kuykendall and Michelle Hickner, Department of Mechanical Engineering, for their time and expertise in manufacturing and testing specimens required for this research. Additionally, I would like to thank Ed Connery, Graduate Advising, for his support and consideration from the beginning of my time at the University of Washington. I would also like to thank the United States Air Force for granting me the opportunity to attend the University of Washington and further my own education. Finally, I would like to thank my family and countless friends for their endless love and support throughout my entire academic journey.

This research was supported by INNOPOLIS Foundation grant funded by the Korean government (Ministry of Science, ICT & Future Planning, Grant number: 14DDI084) through SM Instruments Inc. We also acknowledge the research grant from the Joint Center for Aerospace Technology Innovation (JCATI) from Washington State in the USA.

Chapter 1

INTRODUCTION

> *"Man's flight through life is sustained by the power of his knowledge."*
>
> Austin 'Dusty' Miller

In aerospace, civil, and mechanical engineering applications, it is imperative to ensure structural integrity through the detection and characterization of damage and defects. The presence of defects, such as cracks, dents, corrosion, delaminations, or numerous other forms of damage, can significantly reduce the inherit properties and performance of a structure, thereby increasing the chance of premature failure. Therefore, structural health monitoring (SHM) and nondestructive evaluation (NDE) have been subjects of intense studies in recent decades. In particular, increases in the use of advanced materials, sensors/actuators, and manufacturing processes has spurred the development of numerous SHM/NDE techniques. These methods include – but are not limited to – thermography, shearography, X-radiography, eddy current, ultrasonic C-scan, scanning laser Doppler vibrometry, and guided wave-based ultrasound techniques [1][2][3][4][5]. They are based on thermal, electromagnetic, acoustic/mechanical, and other multi-physical feedback, and each technique offers unique advantages and shortcomings.

Using acoustic emissions for purposes of detecting and localizing damage has been one of the widely adopted methods in the SHM/NDE community [6][7][8]. Acoustic emissions are manifest when a material is subject to extreme stress conditions due to external loads, such that a local point source within the material suddenly releases energy in the form of stress waves. The released stress waves are transmitted to the surface of the material and then propagate outwards from the epicenter of the release source. It is the radiation of the transient elastic waves across the surface of the material that defines an acoustic emission. Previous studies on acoustic emission have focused primarily on the onset of such acoustic emissions to locate their release sources [9][10][11][12]. However, more useful can be that acoustic emissions are also attenuated, scattered, or reflected by discontinuities present in the material [8]. We identify that it is this particular property of acoustic emissions that can be exploited in order to detect and localize pre-existing damage in an inspection medium.

The contents of this thesis will address the following topics. Chapter 2 contains a more in-depth discussion of acoustic emissions and the benefits of using this approach in addition to an introduction to the time-domain delay-sum beamforming theory and a discussion of how this concept is incorporated into the study contained herein. Chapter 3 describes the experimental setup used for monitoring inspection specimens and plates and specifications on how the sound camera was utilized in the study. Chapter 4 gives a detailed discussion of how post-processing results were obtained and walks through specific processes considered and employed during data reduction. Chapter 5 presents the results and findings from the study. Additionally, discussion and interpretation of the results are provided. Finally, Chapter 6 offers concluding remarks and outcomes obtained from the study and experiments. Furthermore, future directions for expanding this research and the utility of the acoustic emission approach are given. As material systems in aerospace manufacturing and commercial industry continue to push technological bounds, it is imperative that inspection techniques are simultaneously advanced and developed to ensure the integrity of these structures and the safety of those who rely on them. Acoustic emissions is one of many techniques that poses the potential to provide inspection capabilities necessary for safe and reliable utilization of next-generation materials and structures.

It should be noted that the information contained in the following chapters has been used for producing several additional publications. These publications are given in references [24][25][26].

Chapter 2

BACKGROUND AND THEORY

> *"Education is the most powerful weapon which you can use to change the world."*
>
> Nelson Mandela

In this chapter, current structural health monitoring and nondestructive evaluation techniques are addressed followed by a brief review of acoustic beamforming. After establishing the foundation of the beamforming method, a detailed analysis of acoustic emissions and the beamforming approach is offered.

2.1 Introduction to Structural Health Monitoring and Nondestructive Evaluation Techniques

The ultimate goal of any structural health monitoring or nondestructive evaluation technique is to detect and characterize damage or defects within materials or structures. In any structure, damage occurs as a result of a microstructural change within the material [13]. This change causes the local material properties to change thereby introducing a discontinuity into the material or structure. Regardless of the technique and whether it is being used during the manufacturing process or for an in-service inspection, the damage detection capability of the method relies on the ability to detect altered material properties associated with the damage location. While often used interchangeably, for the purposes of this study structural health monitoring and nondestructive evaluation will define two different aspects of material monitoring. Structural health monitoring is associated with real-time monitoring of the material or structure. Structural health monitoring techniques are those used to observe the material while it is simultaneously subjected to external stimuli such as compression or tensile forces, shearing forces, etc. In this way, structural health monitoring is detecting "active" forms of damage as they are manifest and propagating. Nondestructive evaluation techniques are tasked with detecting damage in materials that is caused by previous exposure to external stimuli. Unlike structural health monitoring, nondestructive evaluations methods attempt to detect more "passive" forms of damage that are present in materials but are not being creating during the evaluation period. The combination of structural health monitoring and nondestructive evaluation techniques will allow for a comprehensive assessment of the material integrity throughout its lifespan.

There currently exist numerous techniques for performing structural health monitoring and nondestructive evaluation inspections. The most basic of the techniques is the visual test. Relatively self-explanatory, visual testing involves an operator observing the material or structure surface for any apparent defects. While visual inspection is often performed with just the human eye during manufacturing or walk-around inspections of structures, various optical devices such as magnifying glasses, boroscopes or charge-coupled devices (CCDs) can be implemented to enhance the capabilities of a simple visual inspection. Electromagnetic testing methods, specifically Eddy Current testing, involve subjecting a conductive material or structure to an electric current or magnetic field and measuring resultant currents. When the electric currents or magnetic fields encounter a discontinuity, the flow pattern of the current will be altered from the established steady-state conditions alerting the operator to the presence of damage. One of the most widely used techniques is ultrasonic testing encompassing both b-scan and c-scan methods. Ultrasonic methods utilize high-frequency sound waves that are introduced into the material. As the sound waves travel through the material, they do so at a velocity that is correlated to the acoustic impedance of the material. If the acoustic impedance of the material is changed due to the presence of a defect, the sound waves will be reflected back to a receiving device. The advantage of these systems is that by knowing the time of flight of the sound waves through the material based on the velocity of the sound waves, the exact depth of a discontinuity can be determined within a structure based on the difference in time of arrival of the emitted wave and the reflected wave due to the damage. Lastly, thermal and infrared testing utilize the thermal properties of a material. These methods measure the infrared radiation emitted from a material when subject to external heating sources. The methods presented herein enable a conclusion to be drawn about many of the inspection methods. Nearly all methods rely on a singular material property such as electrical conductivity, thermal conductivity, or acoustic impedance for detecting discontinuities within the material. This results in some methods being limited in their ability to detect a fully spectrum of damage modes or being restricted in their application to certain materials; for instance, heat can damage many composite systems and therefore many prohibit the use of thermal inspection methods. While the methods presented are by no means a comprehensive list of available techniques, they serve to demonstrate the wide range of techniques used and highlight that all methods have both advantages and disadvantages. More information and techniques can be found at [4][14].

In addition to visual testing, acoustic-based methods are some of the oldest and most widely used techniques for purposes of structural health monitoring and nondestructive evaluation. Acoustic emission testing was originally developed in conjunction with a standard tap test where a small impact is introduced into a structure or material. The impact causes the material to emit a characteristic acoustic feedback based on the inherit material properties and the acoustic impedance. If a discontinuity is present, the frequency of the acoustic feedback will change notifying the inspector to the presence of damage. While many of the inspection methods mentioned have experienced significant improvement in their testing equipment and reliability, acoustic emission testing has lagged behind in its implementation of modern technology to bolster the capabilities of the method. This research seeks to advance the field of acoustic emission testing for use in damage detection and localization by coupling this technique with a sophisticated air-coupled acoustic array. The hope is to enhance the capabilities of acoustic emission testing and demonstrate the efficacy of this method for use in structural health monitoring and nondestructive evaluations.

2.2 Introduction to Acoustic Emissions

The fundamental properties associated with acoustic emissions have been studied extensively throughout the years. Acoustic emissions are manifest when a material is subject to external stimuli such as an applied tension or compression. When subject to a stress, the material will experience a strain representing the change in shape of the material due to the applied stress. The strain can assume one of two forms, elastic or plastic. If the applied stress is great enough, plastic strain will occur resulting in permanent deformation of the material or structure. Considering the microstructural level, a plastic deformation causes atomic planes to slide over one another through the agency of atomic-scale dislocation [8]. These micro-level dislocations translate to macro-level damage forms such as cracks, delaminations, dents, etc. that all act as precursors to ultimate failure of the material system. The onset of damage results in a local point source within the material releasing energy. The energy released is transmitted to the surface of the material in the form of stress waves and then propagates outwards from the epicenter of the release source. It is the radiation of the transient elastic waves across the surface of the material that generates an acoustic emission [15]. The basic principle is shown in Figure 2.1(a) in addition to a typical detection device that includes a contact sensor attached to the inspection material. It is the acoustic emissions caused by the precursory damage forms which are of great interest in structural health monitoring and nondestructive evaluation.

The amount of energy released at the source is directly correlated to the amplitude of the acoustic emission. Furthermore, the velocity of the microstructural change and the area that it covers are directly proportional to the acoustic emission produced. High velocity microstructural changes coupled with large spatial propagations will result in large amplitude acoustic emissions [8]. For the study presented in this thesis, a commercially available sound camera was used for detection and characterization of the monitored acoustic emission events. The utilized sound camera is shown to the right in Figure 2.1(b); a more detailed discussion of the sound camera is provided in Section 3.1. Figure 2.1(a) has a red box around the

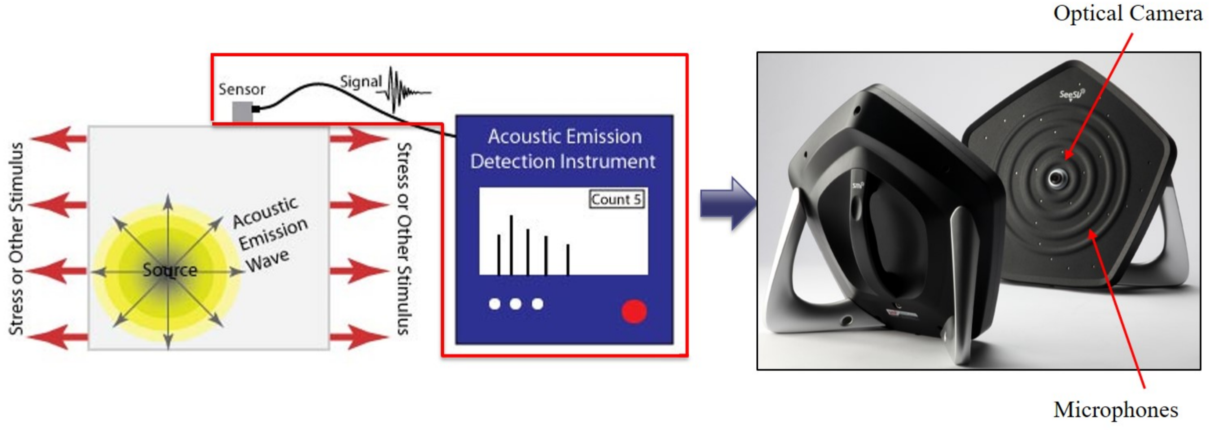

(a) (b)

Figure 2.1: (a) Basis principle of generating an acoustic emission and typical contact sensor equipment used to detect and characterize the acoustic emission. Additionally shown, (b) is the SMI SeeSV-S205 Portable Sound Camera that replaces the traditional contact sensor for detecting acoustic emissions.

conventional contact sensor and detection equipment to signify the system of components that the sound camera replaces. By having a single unit for sensing and detecting the acoustic emission, the sound camera simplifies the equipment setup compared to the conventional contact method for acoustic emission characterization.

One of the most extensively studied forms of damage using acoustic emissions involves the development and propagation of cracks [8]. The major reason cracks are of such interest in the nondestructive evaluation field is that they create new surfaces within the material. The presence of a crack presents a large threat to the integrity of the material system which if significant enough could precipitate premature ultimate failure. Additionally, crack development and propagation generate high amplitude acoustic emissions which are easy to detect and localize making them the primary target of most acoustic emission sensing devices [8]. In addition to the large amplitude acoustic emissions caused by the creation of the crack, small acoustic emissions are emitted from the crack tips during propagation and crack development.

2.2.1 Benefits of Using Acoustic Emissions

While crack growth is the most widely studied damage mode in the field of acoustic emission technology, the nature of acoustic emissions make them a promising technique for much more general structural health monitoring and nondestructive evaluation applications. The acoustic emission beamforming technique coupled with the sound camera device has unique advantages compared to the conventional techniques such as ultrasonic or laser based testing methods [6]. Many of the conventional testing methods are founded on the principle of imparting external stimuli or excitations on the inspection material and measuring differences in the received signal in order to detect whether damage is present and where it is located. While such methods generally provide highly accurate results, they often involve slow and expensive processes to operate equipment. Conversely, acoustic emission beamforming methods can be conducted in situ and in real time, without necessitating permanently mounted contact sensors or baseline data. Recently, laser Doppler vibrometry has gained significant attention as a means to visualize stress waves in solids and structures with an unprecedented resolution. However, this method requires synchronization and reconstruction of data measured from every single discretized spatial point of an inspection medium. This is not practical given the difficulties in exciting structures in a repeated, identical fashion. In contrast, the proposed acoustic emission beamforming technique is capable of conducting non-contact – yet full-field – visualization of inspection medium in a single shot measurement. Consequently, we envision that this method can open new avenues to diagnosing the existence of damage in structures in a time- and cost-efficient manner by conducting simple tapping tests. From a structural health monitoring perspective, acoustic emissions techniques are passive inspection methods (not to be confused with the aforementioned ”passive” damage modes) in that they monitor microstructural changes in the material itself which result in the release of energy compared to other methods that utilize external energy sources to assess the material integrity. This enables real-time monitoring of the material while it is subject to external stimuli without subjecting it to additional external energy sources for monitoring purposes. Furthermore, some of the other inspection methods cannot be used in a real-time monitoring application as they require the inspection material to be isolated such as in a waterbath (some c-span equipment) during inspection. The monitoring of energy releases from the material also means that acoustic emissions are affected by dynamic changes in the material. Consequently, acoustic emissions are dynamic processes and can therefore be used to distinguish between stagnate and propagating damage.

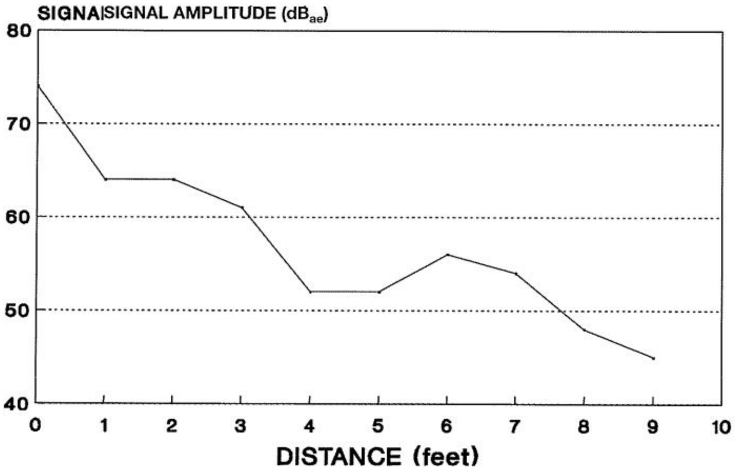

Figure 2.2: Acoustic emission signal amplitude attenuation with respect to distance from source of the acoustic emission [8].

As stated, acoustic emissions are defined as the radiation of transient waves propagating along the surface of a material. Transient waves are known to travel long distances from their origin. This enables large spatial domains to be simultaneously monitored or inspected using a single acoustic emission detection device. Figure 2.2 shows a graphical representation of the acoustic emission signal attenuation as a function of the distance from the emission source. In the majority of structures, attenuation of the signal can be attributed to one of several factors including geometric spreading, scattering due to boundary effects, and absorption [8]. Geometric spreading refer to the wave ”trying” to propagation through the structure [8].

The geometry of the structure will ultimately determine the rate of attenuation due to geometric spreading. For plate like structures, such as those used for inspections in this study, the attenuation rate is approximately 30 percent as illustrated in Figure 2.2. Geometric spreading will ultimately determine the distance from an acoustic emission source at which a discontinuity in the material can be detected. The second major cause of attenuation is due to scattering at the material boundaries. Anytime the transient wave encounters a discontinuity, a portion of the wave energy will be reflected or scattered. This property is especially important in nondestructive evaluation applications as it is the altered wave propagation due to the discontinuity that will help to identify and localize the damage within the material. The last mode of attenuation is due to absorption by the inspection material. During absorption attenutation, transient wave energy is absorbed by the material through which the wave is traveling and converted into another energy form such as heat [8]. Unlike the variable attenuation rate of geometric spreading (higher near the source and lower in the farfield), absorption rates are constant across the spatial domain. This means that near the source, geometric spreading will be the primary source of attenuation while absorption will affect the wave amplitude to a greater degree in the farfield.

The dynamic characteristic of acoustic emissions make them an attractive alternative to other methods for structural health monitoring applications. Because acoustic emissions are produced from within the material system, the use of acoustic emission monitoring enables in situ inspections under various external loading conditions. All modes of attenuation demonstrate that during transmission of the elastic waves, the acoustic emissions are subject to inherit material properties. The dependency on material properties is what makes acoustic emissions so attractive as a nondestructive evaluation technique. The generation of modified acoustic emissions due to discontinuities permits various forms of damage to be detected and isolated within a variety of material systems.

2.3 Time-Domain Delay-Sum Beamforming

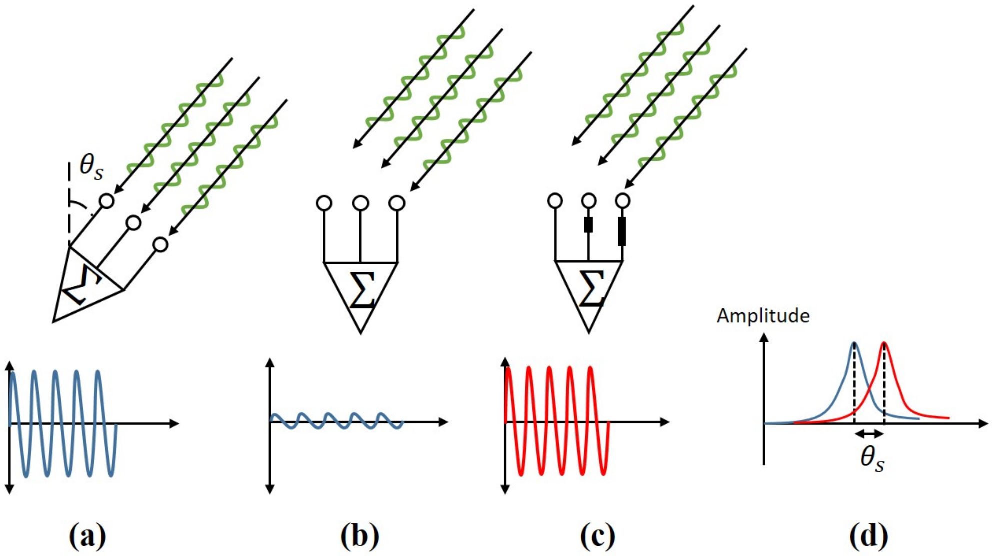

Figure 2.3: Conceptual illustration of beamforming technique. This image is based on a conceptual diagram from reference [20].

Traditional methods of source localization via acoustic emissions rely on the assumption that the recording device is pointed at or aimed in the general vicinity of the emission source. Acoustic beamforming is an attractive alternative for use in acoustic feedback structural health monitoring and nondestructive evaluation as it provides the opportunity to detect the direction of unknown acoustic emissions due to failure events across a large spatial domain [18]. Figure 2.3 shows the concept of determining the location of a signal source using the signal processing technique of acoustic beamforming. Figure 2.3(a) depicts a traditional microphone array aimed in the direction of sound source located at an angle θ_s with respect to the normal direction of the array. When the array is aimed directly at the emission source, the acoustic output is maximized as represented by the resultant microphone output. Figure 2.3(b) shows that same standard microphone array, but now aimed in the normal direction that is askew to the same sound source. The impact of this array shift is reflected in the significantly reduced microphone output. Figure 2.3(c) represents a microphone array that employs a beamforming technique. While the array is aimed in the normal direction at the angle θ_s to the signal source, by implementing delays to each microphone in the array, the microphone output can simulate that of the traditional microphone array aimed at the sound source. By imposing specific signal delays to a sensor array of omni-directional microphones, the directionality of an emitted or received acoustic signal can be controlled. By knowing the delays used for each microphone in the senor array, the phase delay of the signal can be converted to a spatial position in terms of direction and distance of the sound source [20]. In the case shown in Figure 2.3, the phase delays associated with the beamforming technique result in the offset array amplitude signals observed in Figure 2.3(d). It is this offset that can be translated to the direction of the signal source at θ_s as shown.

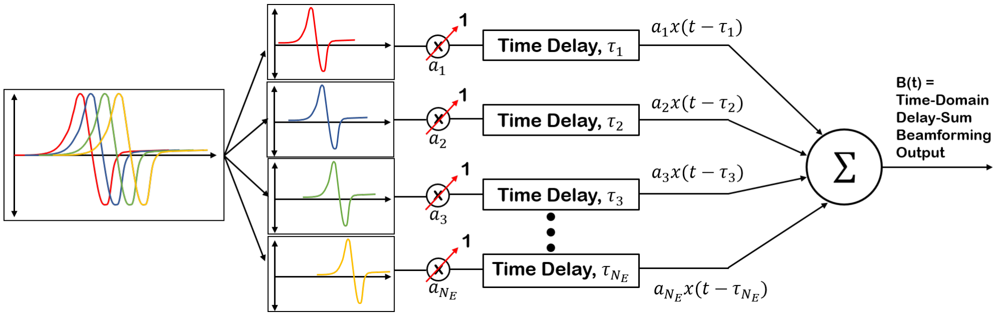

Figure 2.4: Time-domain delay-sum beamformer. This diagram is modified based on a figure in reference [17].

While acoustic beamforming is a relatively new concept for applications related to damage localization, beamforming using microphone arrays is a standard practice for spatial isolation of sound sources. The beamforming method - also known as microphone antenna, phased array of microphones, acoustic telescope, or acoustic camera - is used extensively for localizing sounds on moving objects and to filter out background noise in acoustically active environments with stationary sound sources [19]. Figure 2.4 gives a visual representation of the basic time-domain delay-sum beamforming method. This process can be expressed mathematically by Eq. (2.1) in terms of the time-domain delay-sum beamforming output [17].

$$B(t, \overrightarrow{X}_P) = \sum_{n=1}^{N} a_n x_n[t - \tau_n(\overrightarrow{X}_P)] \tag{2.1}$$

where N is the total number of microphones, t is time, and $\overrightarrow{X}_P = (x_P, y_P, z_P)$ represents the position onto inspection plate with respect to the reference position (e.g., center of the microphone arrays, $\overrightarrow{M}_R$=(0,0,0)). The a_n is a spatial shading or weight coefficient that can be applied to the individual microphones to control mainlobe width and sidelobe levels [17]. In many instances, the weighting coefficients are set to unity or equal to one. $x_n(t)$ represents the acoustic emission received by the n^{th} microphone emitted by an arbitrary sound source.

After receiving the signal, a specified delay, τ_n, is imposed to the signal for each individual microphone based on the spatial domain. Figure 2.5 shows the operation used for calculating the microphone delays. First, the spatial domain of interest is discretized into "pixels" rendering a superimposed grid onto the spatial domain. Second, for each point on the spatial domain the position vector $\overrightarrow{X}_{Ref} = (x_R, y_R, z_R)$ from the spatial pixel $\overrightarrow{X}_P = (x_P, y_P, z_P)$ to a predetermined reference point $\overrightarrow{M}_R = (0, 0, 0)$ is calculated. Also, the position vector of that same spatial pixel to the n_{th} microphone who position is given by $\overrightarrow{M}_n = (x_n, y_n, z_n)$ is determined as $\overrightarrow{X}_{Mic} = (x_{mic}, y_{mic}, z_{mic})$ by $\overrightarrow{X}_{Ref}$ - $\overrightarrow{M}_n$. Finally, the difference of flight time of the acoustic signal between the two vectors is found by calculating the difference in vector magnitudes and dividing the speed of sound c. The time delay for each point on the inspection plate and each n_{th} microphone is defined by Eq. (2.2).

$$\tau_n(\overrightarrow{X}_P) = \frac{1}{c}\left(\left|\overrightarrow{X}_{Ref}\right| - \left|\overrightarrow{X}_{Mic}\right|\right) \tag{2.2}$$

The scanning algorithm of the microphone array will perform the delay calculation operation for the entirety of the spatial domain which it is monitoring. After the time delays for all microphones are imposed on the signal for a given spatial "pixel", the transformed signal from each microphone is summed as shown in Figure 2.4. The location of the

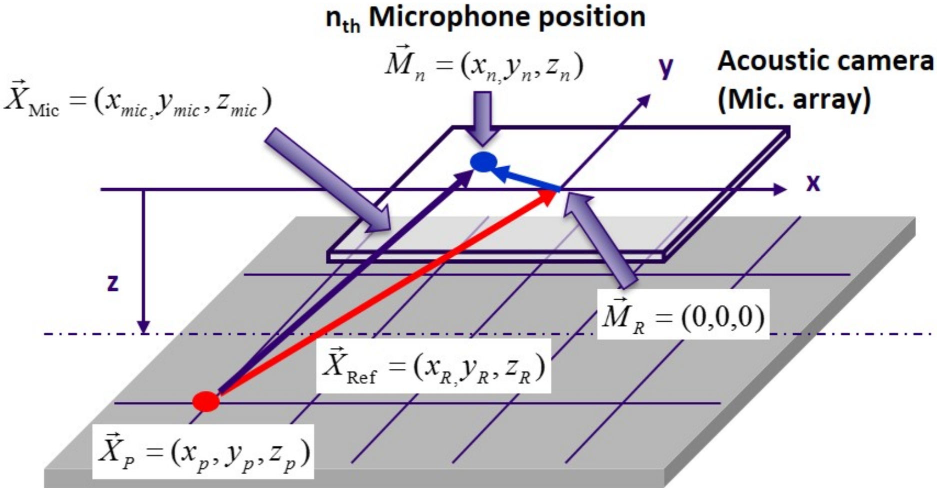

Figure 2.5: Illustration showing concept of calculating delays for a specific microphone for a given spatial position.

sound source is determined by the delays for a specific spatial location which produced the maximum beam output, $B(t)$. It is important to note that the microphone delays are time independent and therefore will remain constant for a given microphone to a given spatial "pixel" throughout the monitoring period assuming the geometry of the test setup remains constant. While Figure 2.4 and Equation 2.1 illustrate the basic delay-sum beamformer in the time-domain, there exist many variations and modifications to this algorithm, see reference [17].

Chapter 3

EXPERIMENTAL SETUP AND METHODOLOGY

> *"It is the mark of an educated mind to be able to entertain a thought without accepting it."*
>
> Aristotle

This chapter will introduce the technical specifications of the SM Instruments SeeSV-S205 sound camera used in this study. Furthermore, details of the experimental setup configurations used for both the structural health monitoring and nondestructive evaluation phases of this study are described in depth throughout the course of this chapter.

3.1 Introduction to SM Instruments SeeSV-S205 Sound Camera

In this study, we used a commercial acoustic emission sensing device equipped with microphone arrays and a motion camera (SeeSV-S205 Sound Camera, SM Instruments). Specifically, the sensing device consisted of a high resolution optical camera with a sampling rate of 25 frames per second (FPS) embedded in the center of the device. The optical camera is surrounded by 30 high sensitivity digital micro-electric mechanical system (MEMS) microphones with a sampling frequency of 25.6 kHz arranged in five helical patterns of 6 microphones each. Figure 3.1 shows the configuration of the sound camera. Figure 3.1(a) shows the internal arrangement of the optical camera surrounded by the helical arrays of microphones. Figure 3.1(b) shows the relative positions of the microphones in relation to the optical sensor located at the center of the array.

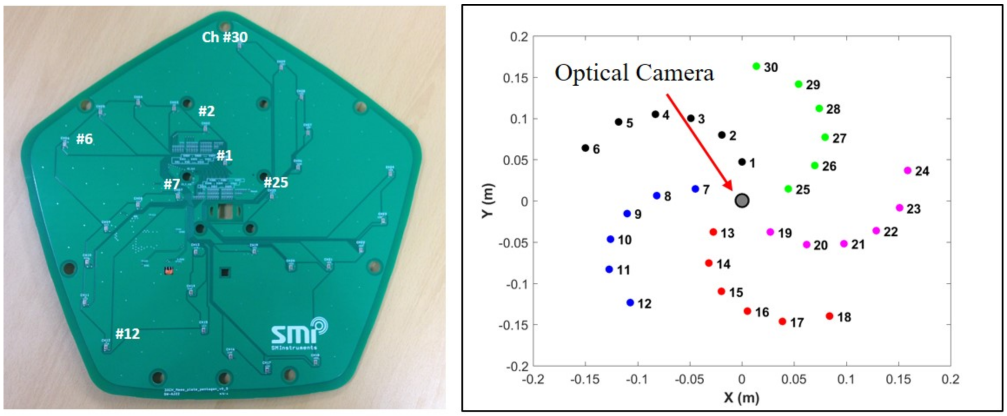

(a) **(b)**

Figure 3.1: (a) Internal view of the SeeSV-S205 sound camera showing helical microphone configuration emmanting from optical camera at the center of the device. (b) Relative microphone positions are given with respect to the optical camera at the center of the array.

Table 3.1: SeeSV-S205 sound camera microphone array operating specifications [20].

Microphone Type	Digital MEMS
Number of Microphones	30 arranged in spiral array
Microphone Sensitivity	70 $^{\mathrm{mV}}/_{\mathrm{Pa}}$
Array Diameter	35 cm
Frequency Range	Min = 350 Hz
	Max = 12 kHz
	Recommended = 2 kHz - 10 kHz
Measurement Distance	Recommended = 0.2 m - 5 m
Sampling Rate	25.6 $^{\mathrm{kS}}/_{\mathrm{s}}$
Imaging Algorithm	Beamforming (delay and sum)
Imaging Ranging	Automatic/Manual
Operating Temperature	-20 to 50°C
Humidity	10 - 85 %

This design allowed for field programmable gate array (FPGA)-based high-speed beamforming which enabled parallel processing of the raw acoustic data and the optical data [20]. It is during the FPGA scanning sequence that the delay-sum beamforming is implemented across the spatial domain. FPGA-based beamforming coupled with the optical camera results in near-real-time visual representation of acoustic emission events. The additional advantage of using MEMS microphones is the ability to detect high frequency transient acoustic emissions. Table 3.1 gives the manufacturer produced operating specifications for the SeeSV-S205 sound camera.

3.2 Experimental Setup for Structural Health Monitoring Applications

3.2.1 Tensile Test Setup

Tensile testing was performed on unidirectional (UD) T800/3900-2 carbon fiber/epoxy prepreg specimens. Test specimens were prepared in five configurations: UD 0°,UD ±45°, and UD 90° consisting of four plies each and $[0/\pm45/90]_s$ and $[90/\pm45/0]_s$ laminates. The test specimens were cured at 350°F for 2.5 hours in a hot press. Test specimens were then cut to 1/2 inch wide coupons by 10 inch length for 0°, ±45°, and 90° samples. The $[0/\pm45/90]_s$ and $[90/\pm45/0]_s$ laminates were cut to 1 inch wide by 10 inch long coupons in accordance with ASTM D3039 composite tensile testing standards. All specimens were tabbed with fiberglass prior to testing in accordance with DOT/FAA/AR-02/106 *Tabbing Guide for Composite Test Specimens*. This meant four layer tapered tabs for 0°, ±45°, and 90° specimens and eight layer tapered tabs for $[0/\pm45/90]_s$ and $[90/\pm45/0]_s$ laminates.

Tensile loads were applied using an Instron 5585H load frame as shown in Figure 3.2. According to ASTM D3039, the standard load rate is 2 mm/min for tensile tests. However, the sound camera had a maximum recording time of 180 seconds meaning the load rate needed to be altered for some specimens to ensure they reached ultimate failure during the recording time. While 2 mm/min was appropriate for 90° specimens, the load rate needed to be increased to 4 mm/min for 0° specimens and 15 mm/min for ±45° specimens. Both

$[0/\pm45/90]_s$ and $[90/\pm45/0]_s$ laminates were loaded at 10 mm/min.

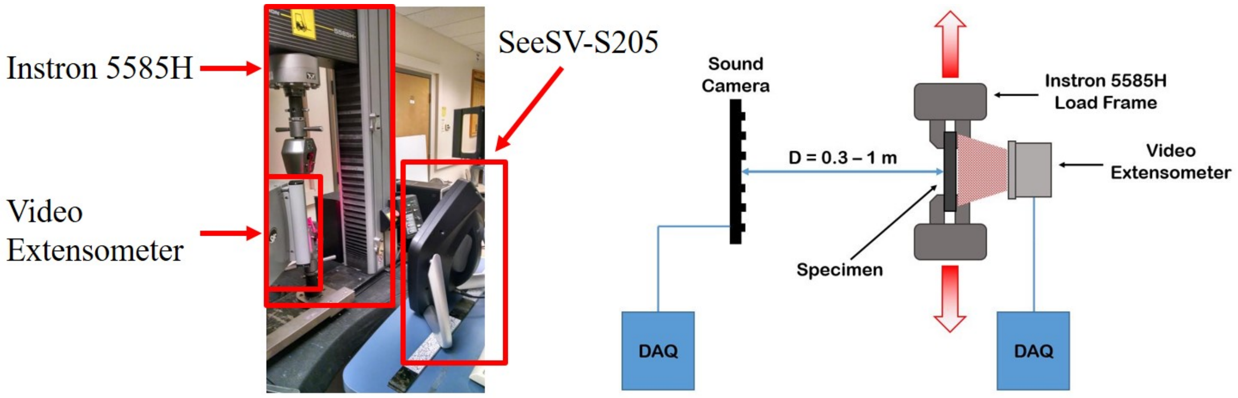

(a) (b)

Figure 3.2: (a) Actual experimental test setup showing the SeeSV-S205 Sound Camera aimed at speciment loaded in Instron 5585H load frame. Specimen also monitored by video extensometer for stress-strain data. (b) Schematic of the experimental test setup showing the range of distances from the sound camera to the inspection specimen and two data acquistion units.

The sound camera position relative to the test specimen was varied during testing as shown in Figure 3.2(b) in order to achieve increased resolution of failure events and location isolation. The sound camera distance from the test specimen was decreased from 1 meter to approximately 0.3 meter during testing. All distances in this range are within in the recommended measurement distance between 0.2 meters to 5 meters as prescribed by SM Instruments. The sound camera was positioned directly facing the vice grips and test specimen in the load frame. Due to use of video extensometry to measure strain data, the specimen was oriented at approximately a 45° angle to the sound camera as seen in Figure 3.2(a).

3.3 Experimental Setup for Nondestructive Evaluation Applications

In this study, we experimentally demonstrate the feasibility of visualizing stress waves in an aluminum plate by using acoustic emissions. The focus is whether acoustic emission techniques can capture the scattering of stress waves due to the presence of damage resulting from an applied impact on the plate. Note that arrays of microphones have been used in previous studies to identify the locations of vibration sources [16], but it has not been attempted yet to visualize stress waves in structures via air-coupled microphone sensors to the best of the authors' knowledge. This is because of a short characteristic time – in the order of micro-seconds – of stress waves propagating in solids and also due to the difficulty in capturing and visualizing the wavefronts of these stress waves.

3.3.1 Inspection Plate

Figure 3.3 shows the conceptual experimental setup used in this study to induce and track the transient waves in the aluminum plate. The illustration shows the 1.2192 m × 1.2192 m (48 in × 48 in) 6061-T6 aluminum plate mounted to an optical table using a rail system to create a fixed boundary condition around the plate. The boundary system consisted of 1 in × 1 in square 6061-T6 aluminum tubing and 1 in × 1 in 6061-T6 aluminum angle bars. The plate was secured between the angle bars and the square tube with fasteners placed every 6 inches that went through all pieces to effectively fix the boundary of the plate and suspend it above the optical table. We used two different thicknesses of the plate, 1.02 mm and 6.35 mm, to assess the capability of the sound camera to detect the variable wave propagation velocities.

Once the plate was installed, the acoustic camera was mounted above the center of the plate at a height of approximately 0.520m. Impacts were introduced into the plate via manually tapping the plate using the tip of a hexagonal wrench while simultaneously capturing the acoustic signal recorded by the 30 microphones. Afterwards, post-processing was performed to calculate the time delays and beamforming output based on Equations

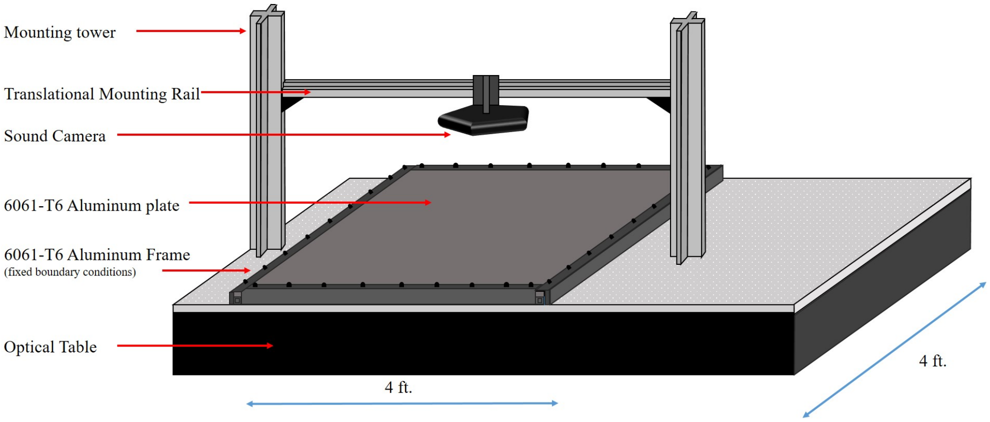

Figure 3.3: Proposed experimental setup for inducing and tracking transient wave in aluminum plates using acoustic microphone array.

(2.1) and (2.2) in order to produce the acoustic images.

Figure 3.4 shows the actual experimental setup used for testing. Figure 3.4(a) shows the aluminum 6061-T6 square tubing used to suspend the inspection plate above the optical table. With the inspection plate secured between the square tubing and angle bars, this effectively created a fixed boundary condition on the plate. Figure 3.4(b) shows the acoustic damping pad made from cloth breather material that is placed under the inspection plate to reduce echos created in the cavity between the suspended inspection plate and the optical table. Figure 3.4(c) and Figure 3.4(d) show the entire experimental setup used for testing with the sound camera mounted above the center of the plate and the inspection plate secured firmly to the optical table. Several iterations of the shown test setup were used with different impact locations, plate thicknesses, and masses placed at various points across the plate to characterize the capability of the sound camera and beamforming technique for detecting discontinuities in the plate under various scenarios.

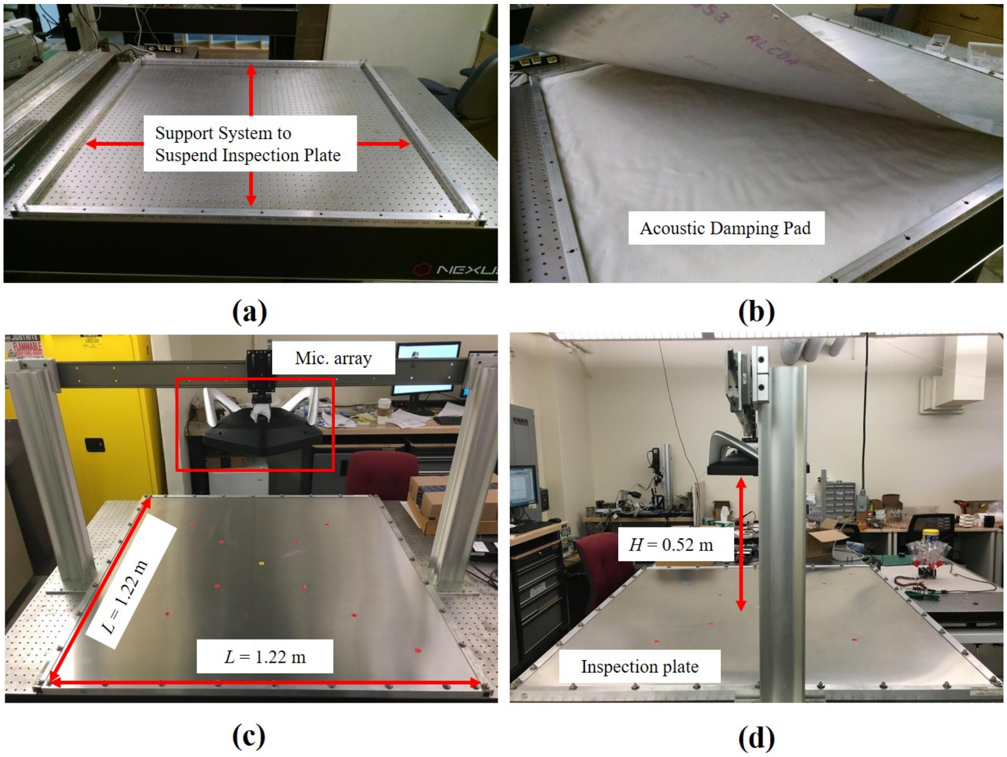

Figure 3.4: Actual experimental setup with no mass present on the plate. (a) Square tubing used to suspend the aluminum plate above the optical table. (b) Acoustic dampening pad placed between the inspection plate and optical table to reduce echos created from the impact. (c) Front view of the mounted inspection plate with the acoustic camera suspended above the plate. The red dots are used to mark impact and mass locations and the yellow dot is the center of the plate. (d) Side image of the experimental setup showing the acoustic camera is centered above the inspection plate and mounting height of 0.52 m.

Chapter 4

DATA ANALYSIS

> *"The function of education is to teach one to think intensively and to think critically. Intelligence plus character - that is the goal of true education."*
>
> Martin Luther King, Jr.

This chapter will outline the post-processing procedures used for structural health monitoring and nondestructive evaluation applications. The discussion will include references to MATLAB code used for the post-processing that is contained in the Appendix.

4.1 Post-Processing of Tensile Testing Results

As shown in Figure 3.2(b) depicting the test setup schematic used for the structural health monitoring phase of the study, two different data acquisition systems were used to monitor the specimen. The raw optical footage from the SeeSV-S205 Sound Camera was captured throughout the loading period. The camera recording was started approximately 3-5 seconds prior to loading being applied to the specimen to ensure that the beginning of the loading profile was captured by the camera. As soon as loading was applied to the specimen, another data acquisition unit was used to simultaneously record the stress-strain data for the specimen as recorded by the video extensometer. This section explains the data correlation and data analysis used for assessing the acoustic emission events recorded by the camera and how that data was ultimately quantified.

4.1.1 Load Optical and Stress-Strain Data

Appendix A.1 gives the MATLAB code used for loading both the optical data recorded from the SeeSV-S205 Sound Camera and the stress-strain data from the video extensometer. In the code given, sound camera and stress-strain data for a $[0/\pm45/90]_s$ specimen is being loaded. The stress-strain data was accompanied with time and loading data and therefore lines 9 and 10 of Appendix A.1 are declaring the data sets containing stress-strain data.

4.1.2 Initialize Video File and Time-Correlate Data Sets

The primary purpose of Appendix A.2 is to initialize the video file for writing the post-processed and analysis data to, but more importantly to time-correlate the sound camera data and the stress-strain data. As the sound camera recording was initialized prior to loading being applied to the specimen, the start of the video footage needed to be cut to ensure the first optical frame was at the moment loading began. Line 1 of Appendix A.2 determines the starting frame for the video footage. The factor of 2.5 applied to the data length is because the sound camera optical data was collected at 25 frames per second while the video extensometer recorded stress-strain data at a rate of 10 Hz. Therefore the video data needed to be 2.5 times longer than the stress-strain data to cover the entire loading period. Once the starting frame of the video data is determined (kstart), the first video frame as recorded by the sound camera optical camera is read in (lines 9,8).

4.1.3 Refine Inspection Window and Plot Recorded Acoustic Emission Events

Appendix A.3 deals with the analysis of identified acoustic emission events and marking them on the stress-strain plot. Lines 1-4 are refining the inspection window. Figure 4.1 shows the results of the inspection window refinement and is used as a way to filter out background and environmental noise from the analysis (granted, noise could still penetrate the inspection window but this procedure drastically reduced marking of non-damage related acoustic emissions). Because the sound camera illustrated acoustic emissions with color contours as shown in Figure 4.1, once the window was narrowed a criteria based on color levels detected in the RGB scale was established to determine if an acoustic emission event had occurred. Lines 5-8 show that the red and blue color spectra were used for this criteria. Both were used to make the criteria more sensitive to smaller acoustic emission events as only using a single color channel meant that cutoff levels had to be so high that small amplitude events were missed. Lines 5 and 7 scan the given refined frame and determine the level of red and blue in the frame, respectively. Lines 6 and 8 are the cutoff criteria stating that if red and blue color saturation levels are greater than 80 and 65, respectively, than it is concluded that an acoustic emission event is being shown in the inspection window.

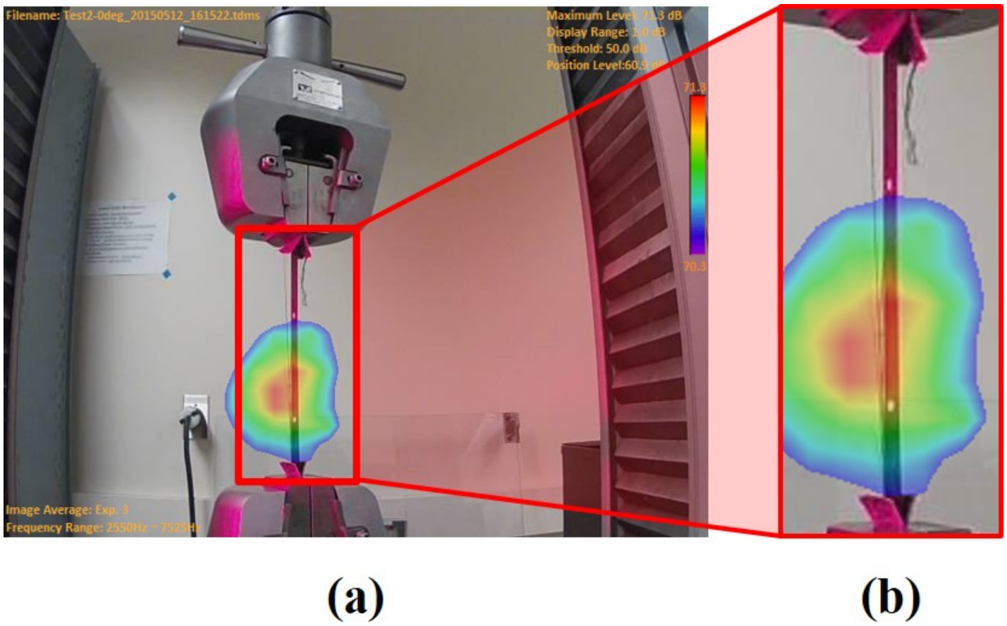

Figure 4.1: (a) Original raw optical image from the SeeSV-S205 Sound Camera for camera placed approximately 1 m from the test specimen. The red box indicates the area of interest for acoustic emissions which are shown by the color contours. (b) Enlarged view of the inspection window showing acoustic emission resulting from fiber breakout.

If it was determined that an acoustic emission was detected within the inspection window, the acoustic emission event was marked on the stress-strain plot by a red marker indicating the relative stress-strain level at which the acoustic emission event had been detected. A figure was made with the sound camera optical image of the acoustic emission event placed as an inset on the stress-strain plot (lines 36-37) with markers indicating all identified acoustic emission events (lines 28-33). These figures were recorded into the earlier initialized video file. This resulted in an animation of all acoustic emission events shown in conjunction with the developing stress-strain data.

4.2 Post-Processing of Wave Propagation Results

As shown in Figure 3.4, the sound camera is used to inspect an aluminum plate onto which an impact is induced to create a stress wave propagation across the plate. Once experiments were complete, post-processing was performed to create acoustic images of the wave propagation across the plate. This section outlines the techniques used for implementing the delay-sum beamforming method for visualization of the wave propagation.

4.2.1 Load Data, Refine Sample Window, and Declare Sampling Parameters

Appendix B.1 presents the MATLAB code used for reading in the raw acoustic data gathered from the sound camera and the refinement/cutting of the signal used for subsequent post-processing. After determining the impact location and whether or not a mass would be placed on the inspection plate for a given test, a manually controlled impact was induced into the inspection plate. The SeeSV-S205 Sound Camera was used to collect acoustic information for all 30 microphones for approximately 2 seconds preceding and 3 seconds post-impact. Figure 4.2(a) shows the raw signal collected over the entire recording time for all 30 microphone channels. The spike in the acoustic data marks the detection of the induced impact. Due to the substantial propagation velocity for the transient wave in the aluminum plate, only a small portion of the collected raw signal was needed in order to visualize the wave propagation into the farfield of the plate from the impact location. The black box in Figure 4.2(a) shows the approximate window of the total acoustic data shown in Figure 4.2(b) which was used for the wave propagation visualization. This window was determined by finding the maximum amplitude of the signal across the entire recording period. This peak amplitude was taken to be the instant of impact. In order to ensure that impact was captured, the refined window included 10 samples before the peak sample and 200 samples after the peak sample to allow for sufficient propagation of the wave into the farfield. Additionally, Appendix B.1 is where experimental parameters including sampling frequency, number of microphone channels, and speed of sound in air are declared.

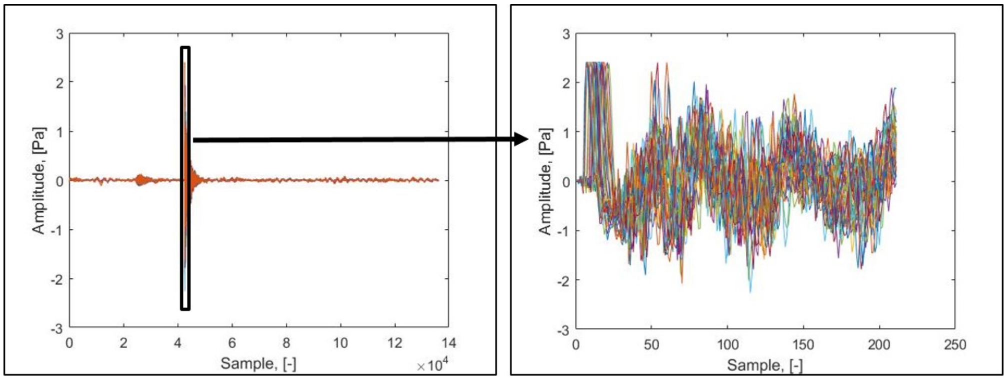

(a)

(b)

Figure 4.2: (a) The raw acoustic signal collected for the impact for all 30 microphone channels showing the acoustic feedback recorded for the impact. (b) Refined and cut acoustic signal used for wave propagation visualization.

4.2.2 Define Area and Discretization of Inspection Plate

Appendix B.2 is where the physical area of the 1.2192 m × 1.2192 m inspection plate is defined. Additionally, Appendix B.2 is used to define the spatial discretization (in terms of number of pixels in each dimension) of the inspection plate which is used in the spatial resolution study and subsequent wave propagation analyses.

4.2.3 Define Microphone Positions with Respect to the Inspection Plate

Appendix B.3 is used to define the microphone positions on the array with respect to the inspection plate. Without considering the height of the microphone array from the plate, Figure 3.1(b) represents the microphone positions defined in this section. However, the x-component of the microphone positions must be opposite in sign so that the microphone array is oriented as if looking down on the inspection plate. Defining the exact microphone positions (including height) is critical as the array position and relative microphone positions will determine the flight times from "pixels" across the spatial domain which are used to calculated microphone delay times. It was noted during post-processing that even small changes in defined location would significantly change time-delays and ultimately affect the wave visualization.

4.2.4 Calculate Microphone Delay Profiles Across the Spatial Domain

Appendix B.4 is the calculation of the delay times as depicted in Figure 2.5. X_{Ref} is the magnitude of the flight vector from the spatial "pixel" to the reference point at the center of the microphone array (optical sensor). X_{Ch} is the magnitude of the flight vector from that same spatial "pixel" to a given microphone on the array. The $Delay_{Sec}$ is the time delay determined from the difference between the reference flight magnitude vector and the position flight vector magnitude to a given microphone divided by the speed of sound in air. Finally, the $Delay_{Samples}$ is the number of discrete samples necessary to adjust the microphone signal to account for the time delay for the given spatial location. This is simply calculated by multiplying the time delay by the sampling frequency of the microphones. This is important to note as this sampling frequency and thus the delay in terms of samples must account for upsample factors in subsequent temporal parametric studies where interpolations are applied to the signal. The time delay profiles across the entire spatial domain for all the individual microphones on the array is given in Appendix C.

4.2.5 Apply Zeropadding to Refined Sample Window

Appendix B.5 refers to applying zeropadding to the refined acoustic sample. Zeropadding is the extension of the acoustic signal on either end by a number of samples equal to that of the greatest delay calculated. These extra samples are all set equal to zero as seen in Figure 4.3(b) and thus the term zeropadding. Zeropadding allowed for the beamforming images

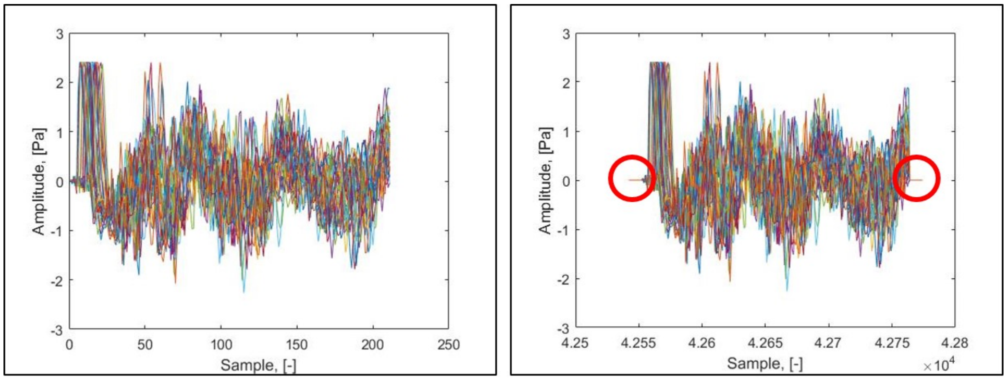

(a) **(b)**

Figure 4.3: (a) Refined raw acoustic signal that was cut from original raw signal. (b) Zeropadding applied to refined raw signal denoted by red circles at the ends of the signal.

to start at the first sample of the refined window without including extra samples from the raw acoustic signal. The reason extra samples are needed or zeropadding must be applied is that delays are both positive and negative depending on the spatial location and given microphone. Therefore, at the first sample used for the beamforming process, there must be samples before it as some microphone channels will have negative delays. Again, while not necessary in this application, it enabled a finer tuning of the refinement window without concern for including enough precursor samples necessary for the beamforming algorithm.

4.2.6 Apply Fast Fourier Interpolation to Refined Sample Window

Appendix B.6 references the frequency-domain fast fourier interpolation applied to the zeropadded signal in order to reconstruct the original acoustic signal with a greater sample rate. The upsample factor in line 4 represents the number of interpolated samples between adjacent samples in the original signal. The built in MATLAB function *interpft* was used to perform the interpolation and signal reconstruction. Figure 4.4 shows a few samples of the much larger acoustic signal for a single channel. The original signal shows drastic amplitude changes between subsequent samples which in addition to high propagation velocities, necessitated

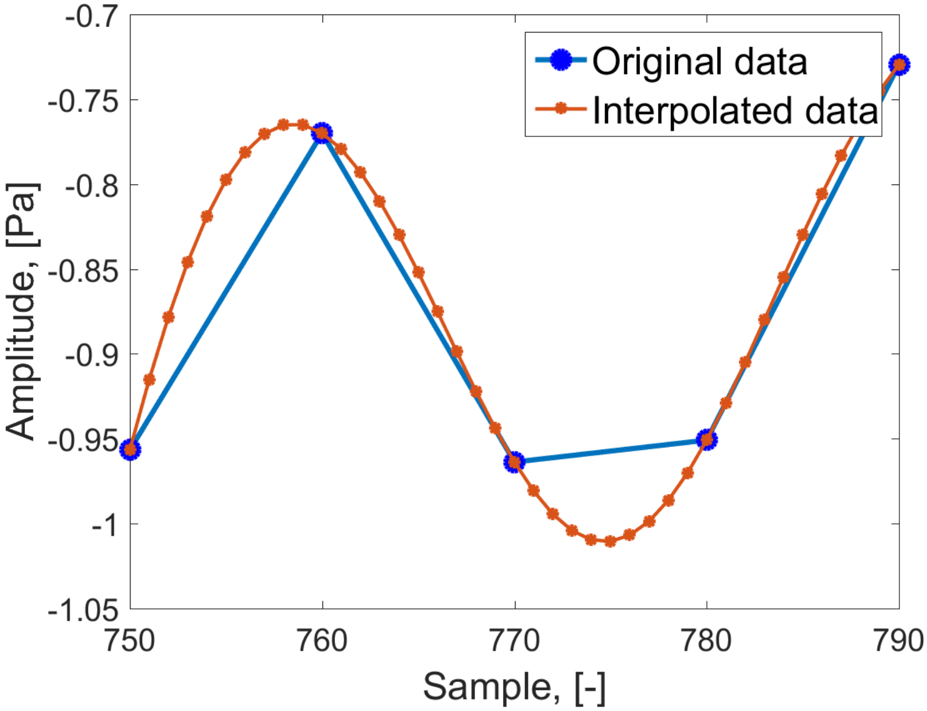

Figure 4.4: Plot of a few acoustic samples to demonstrate the effects of the fast fourier transform signal interpolation and reconstruction using different upsample factors.

the need for signal interpolation and reconstruction. The interpolated signal shows much smoother transition between subsequent samples, elimination of peaks in the signal, as well as a significantly reduced time between samples.

4.2.7 Perform Simple Time-Domain Delay-Sum Beamforming

Appendix B.7 gives the implementation of the acoustic beamforming technique. The start time is given as the first sample of the refined sample window that was determined in Appendix B.1 prior to zeropadding and interpolations being applied. The beamforming algorithm then scans across the spatial "pixels" of the inspection plate and determines the signal strength for each microphone at that spatiotemporal location based on the spatial delays required for the given microphone. Once all signal strengths are determined through adjustment for the time delays, the signals are summed and indexed in both space and time (line 13). This process is iterated through time across all spatial "pixels" to create beamforming images on the inspection plate at each point in the wave propagation sequence.

4.2.8 Plot the Beamforming Image on the Inspection Plate

Finally, Appendix B.8 gives the procedure used for visualizing the actual acoustic beamforming images on the inspection plate and creating an animation of the wave propagation. The first step was to initialize the video file which would ultimately become the animation of the wave propagation. The thing to note in line 2 is the slowed frame rate of the video. Given the MATLAB default frame rate of 30 and the high velocity wave propagation, the videos showing the wave propagation were very short and it was difficult to gather any useful information from them. A slower frame rate allowed the wave propagation to be viewed at a speed which was much easier to follow and distinguish distinctive wave features from. The MATLAB *surf* command was used to visual the wave propagation across the plate as the beamforming acoustic image consisted of an amplitude given in both space and time. Therefore, a surface plot of the beamforming image at a given time was plotted for the entire spatial domain (inspection plate area). One of the characteristics of the wave propagation noted early on was the rapid decrease in the amplitude of the signal post-impact. As a result, lines 17-51 give the adjusted scale used to ensure that wave definition was maintained into the farfield of the plate and that saturation at any given time was minimized. Using an adjustable scale also enabled high resolution of the impact location which would be necessary for subsequent quantitative assessments of the sound camera. The exact impact location and if present, mass locations, were plotted on the beamforming images to assist in assessing the sound camera's ability to properly identify these features. The beamforming images were then saved and imported into a video file before the next image in the time sequence was generated.

Chapter 5

RESULTS AND DISCUSSION

"Testing leads to failure, and failure leads to understanding."

Burt Rutan

This chapter presents results and analysis from structural health monitoring tensile tests and nondestructive evaluation stress wave propagation visualizations. Each of the specimen compositions used in the tensile tests are addressed in detail and detection capabilities are assessed. Conclusions drawn from parametric studies performed for purposes of transient wave visualization are offered. Finally, quantitative results from impact and simulate damage detection and localization investigations are given.

5.1 Results from Structural Health Monitoring Applications

5.1.1 Unidirectional 0° Specimen Testing

Figure 5.1 shows acoustic feedback captured by the sound camera during testing of a unidirectional (UD) 0° test specimen. The color intensity represents the summed amplitude of sound pressure measured by the MEMS microphones on the sensor array. Because fiber breakage is the primary failure mode for a UD 0° laminate, the acoustic feedback events are high amplitude and high energy. This allows for fairly precise localization of the emission source. Figure 5.1(b) demonstrates this accuracy by showing isolation of the sound source associated with the fiber breakout (origin marked with white arrow) on the sample near the epicenter of the acoustic emission.

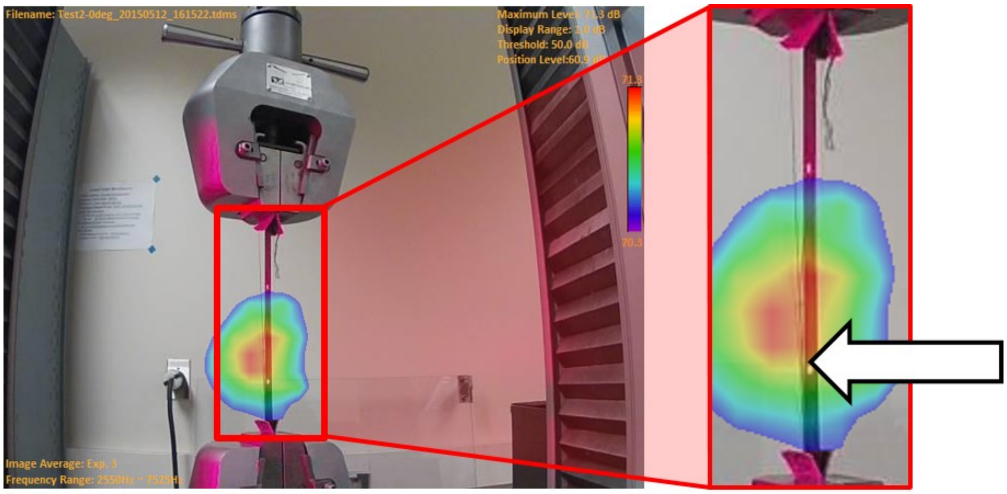

(a) **(b)**

Figure 5.1: (a) Uni-axial tensile testing of unidirectional 0° laminate with fiber breakout detected. (b) Enlarged view of acoustic emission event showing acoustic emission event epicenter near origin of fiber breakout.

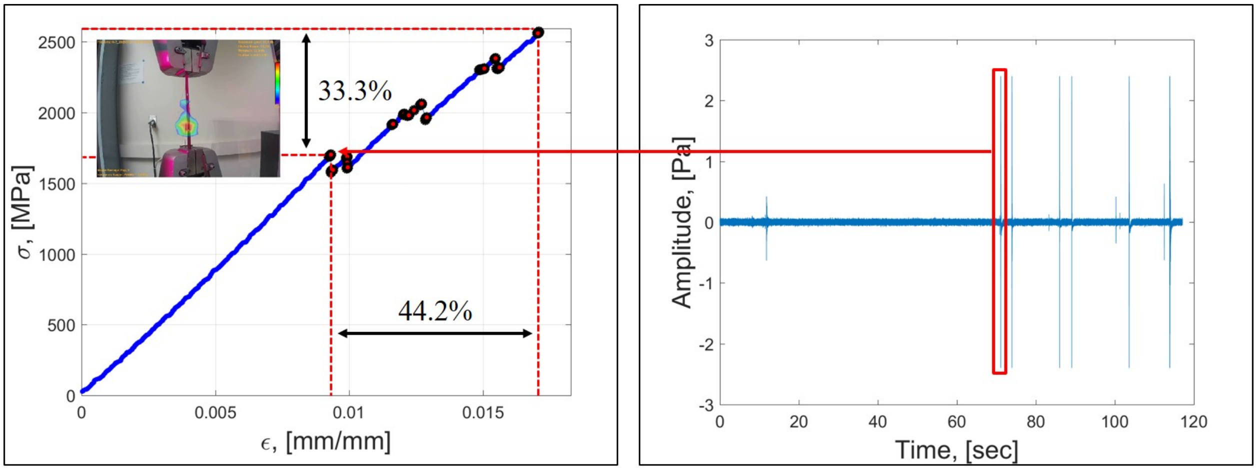

(a) **(b)**

Figure 5.2: (a) Unidirectional 0° T800/3900-2 carbon/epoxy prepreg specimen stress-strain profile with marked failure precursors indicated by acoustic emission events captured by sound camera recording (inset shown). (b) Raw acoustic amplitude data from channel 1 of sound camera recording.

Figure 5.2 shows the test results from one of the many tested UD 0° specimens. Figure 5.2(a) shows the real-time video captured by the sound camera (inset) and the time-correlated stress-strain data collected by means of video extensometry for this specimen. The sound camera video shows the specimen at the moment of failure and is indicated by the red marker in the upper right of the stress-strain data. During correlation of the sound camera video and stress-strain data, video processing was performed in order to mark the stress-strain data anytime an AE event was detected by the sound camera denoted by the red markers. Figure 5.2(b) is a raw acoustic file from the sound camera for this test specimen. Comparing the stress-strain data in Figure 5.2(a) to the raw amplitude data in Figure 5.2(b), all major AE events are captured and marked on the stress-strain plot. This conclusion was draw from visual inspection of the data demonstrated by the red box and arrow which shows the association of raw acoustic events and those events marked on the stress-strain profile. Furthermore, looking at the stress-strain plot in Figure 5.2(a), small steps in the data indicative of failure events are accurately detected and marked by the sound camera. The early spike in Figure 5.2(b) was due to background machine noise detected by the camera. Confident that the sound camera captured the AE events associated with damage in the specimen, the stress-strain data was analyzed to determine the damage detection capabilities of the sound camera. Ultimate failure for this specimen occurs at approximate loading conditions of 0.0165 mm/mm and 2550 MPa. The earliest indicated AE event is shown at loading conditions of 0.0092 mm/mm and 1700 MPa. This data suggests that the sound camera was able to detect failure precursors at approximately 56 percent ultimate failure strain and 67 percent ultimate failure stress. Other UD 0° samples showed similar AE profiles with the sound camera able to accurately detect and localize the source of the damage events throughout the duration of the test.

5.1.2 Unidirectional 90° Specimen Testing

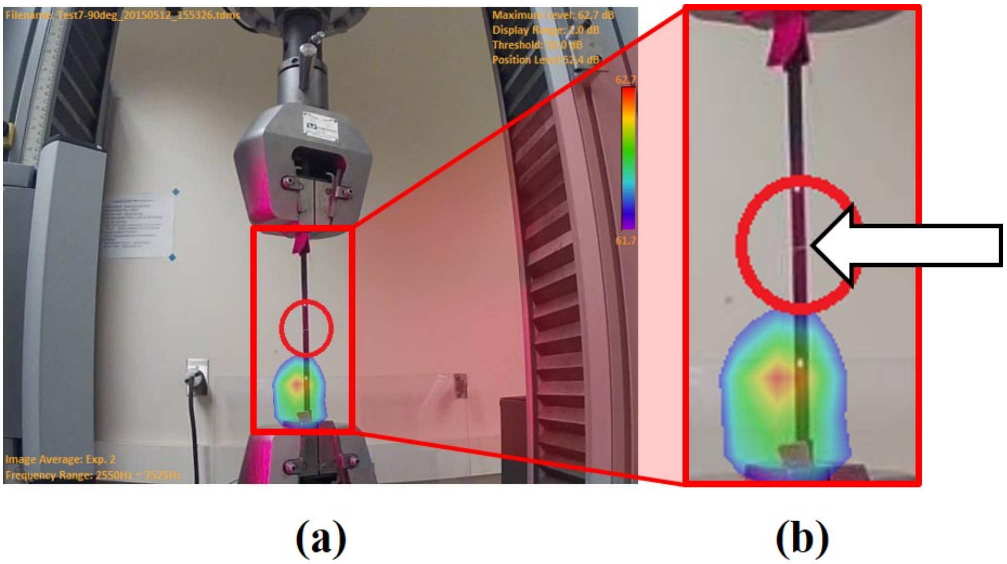

Figure 5.3: (a) Uni-axial tensile testing of unidirectional 90° laminate shown at ultimate failure. (b) Enlarged view of acoustic emission event showing acoustic emission event misrepresenting the failure location indicated by white arrow in center of specimen.

Figure 5.3(a) shows the image taken right at the instant of failure for a 90° UD specimen. While the image locates the sound source near the lower grip, it can be seen in Figure 5.3(b) that the location of failure is in the center of the specimen (location denoted by white arrow) as desired for tensile testing. During testing, it was noted that the 90° samples tended to show an emitted sound source near the grips at failure despite the majority of failures occurring in the middle of the test specimens. As opposed to the UD 0° specimens, the failure of UD 90° specimens is in the form of transverse tensile failure of the matrix. The acoustic feedback associated with this failure mode is of significantly reduced intensity from the tensile failure of the fibers in the case of the 0° specimens. The significantly lower acoustic feedback is likely a contributing factor to the misidentified location of sound emission at failure of the 90° specimens. This does not negate the fact that the sound camera was still able to accurately detect the moment of failure of the 90° specimens during each test due to the acoustic feedback. Further optimization of sound camera settings and the development of filters will likely increase the accuracy of the sound camera for locating failure in lower acoustic feedback settings.

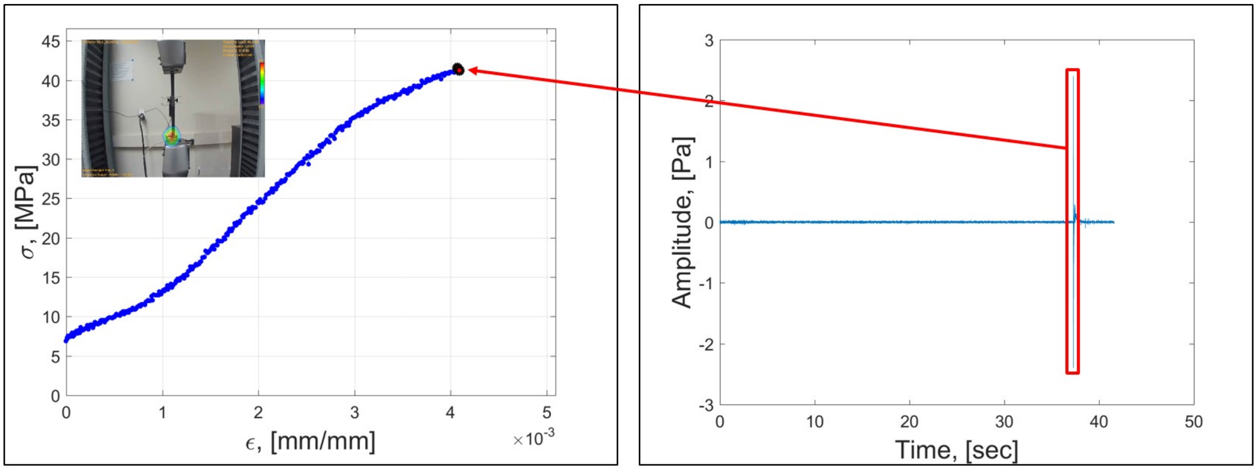

(a) **(b)**

Figure 5.4: (a) Unidirectional 90° T800/3900-2 carbon/epoxy prepreg specimen stress-strain profile with marked failure precursors as indicated by acoustic emission events captured by sound camera recording(inset shown). (b) Raw acoustic amplitude data from channel 1 of sound camera recording.

Figure 5.4 shows the experimental results obtained from one of the several tested UD 90° specimens. Figure 5.4(a) shows the real-time video captured by the sound camera and the time-correlated stress-strain data. During testing of UD 90° and UD ±45° specimens, the video extensometer used to collect stress-strain data for other tests was broken and a clip-on extensometer was used instead. This proved appropriate as Figure 5.4 shows that these specimens showed no failure precursors prior to ultimate failure thereby affecting the accuracy of the extensomer data. The camera image in Figure 5.4(a) shows that in this case the sound camera was able to both detect and accurately isolate the AE source for this specimen. While the sound camera always detected the moment of failure for the UD 90° specimens, the camera struggled to isolate the correct emission source due to the low amplitude AE and slipping of the extensomer caused by failure which caused an additional AE event. In later tests, UD 90° specimens were tested using the video extensomer to assess whether the clip-on extensomer was the source of the isolation issues experienced during testing. In these tests, the sound camera reliably detected the failure event but failed to accurately isolate the source of emission again due to the low amplitude and energy associated with the failure modes of the UD 90° specimens.

5.1.3 Unidirectional 45° Specimen Testing

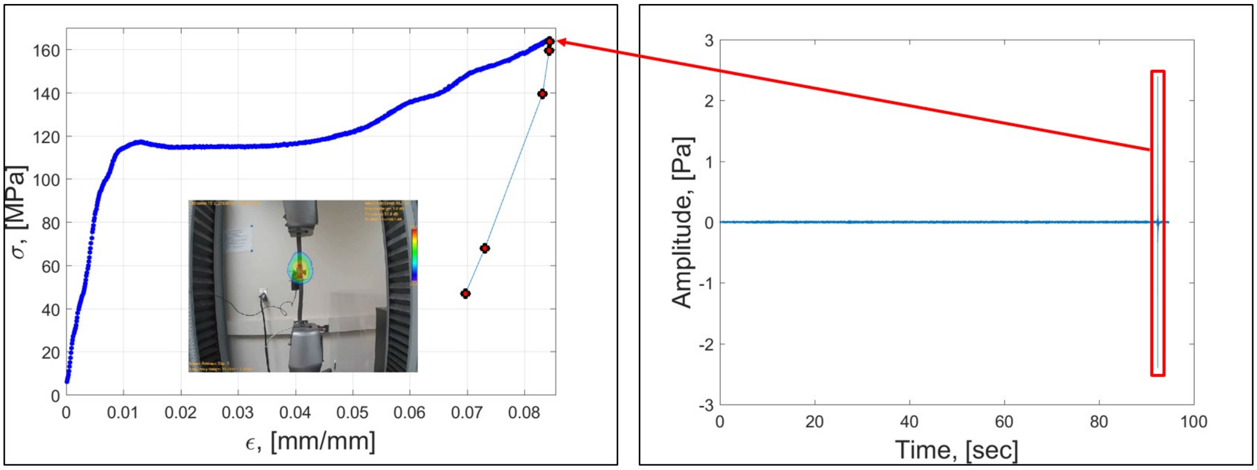

(a) **(b)**

Figure 5.5: (a) Unidirectional ±45° T800/3900-2 carbon/epoxy prepreg specimen stress-strain profile with marked failure precursors as indicated by acoustic emission events captured by sound camera recording(inset shown). (b) Raw acoustic amplitude data from channel 1 of sound camera recording.

Figure 5.5 shows the results from one of the tested UD ±45° specimens. The stress-strain data in Figure 5.5(a) shows the characteristic loading profile for a UD ±45° specimen where scissoring of the layers and fibers occurs causing the stress to plateau prior to loading to ultimate failure. Looking at Figure 5.5(b) it is evident that ultimate failure is the only AE event recorded by the sound camera. The camera image in Figure 5.5(a) shows that the camera was able to capture the AE resulting from failure of the sample. However, the location of this failure was often not accurate for the UD ±45° specimens, similar to UD 90° specimens, due to slipping of the extensometer at the moment of failure.

5.1.4 Unidirectional [0/±45/90]$_s$ Laminate Testing

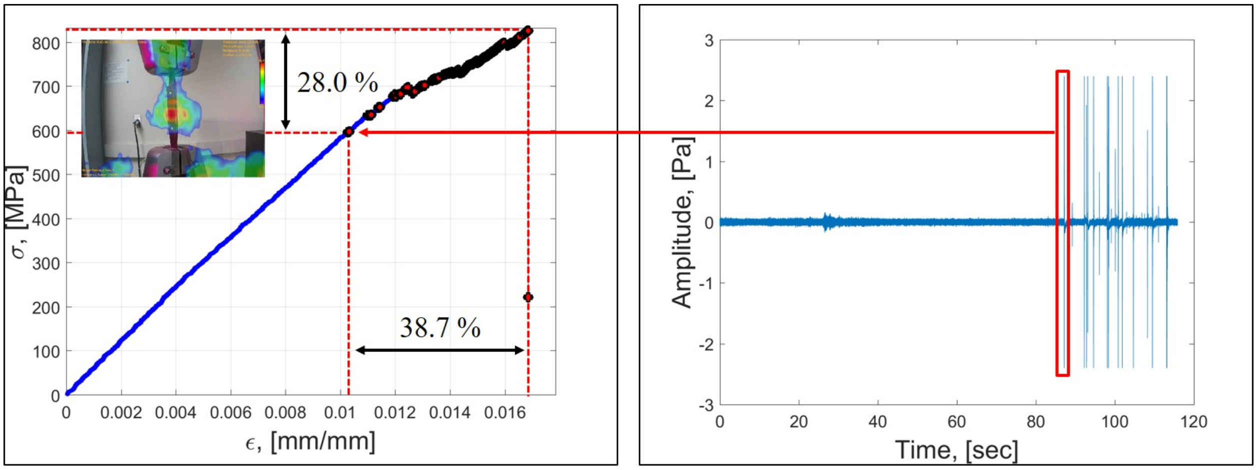

(a) **(b)**

Figure 5.6: (a) [0/45/90]$_s$ T800/3900-2 carbon/epoxy prepreg specimen stress-strain profile with marked failure precursors as indicated by acoustic emission events captured by sound camera recording(inset shown). (b) Raw acoustic amplitude data from channel 1 of sound camera recording.

Lastly, Figure 5.6 shows the test results from one of the [0/±45/90]$_s$specimens. [90/±45/0]$_s$ specimens showed very similar behavior to [0/±45/90]$_s$ specimens and therefore dedicated discussion about them has been omitted for brevity. The sound camera image in Figure 5.6(a) shows the moment of failure of the specimen. The AE is wide-spread as indicated by the sound camera. This is because the majority of the multi-axial laminates experienced catastrophic failure of the laminate at ultimate loading. Fiber breakage and delaminations occurred throughout the sample contributing to the observed delocalized AE. Comparing the stress-strain data in Figure 5.6(a) to the raw amplitude data in Figure 5.6(b), all major AE events leading to ultimate failure appear to be captured and marked on the stress-strain plot. Ultimate failure for this specimen occurs at approximate loading conditions of 0.0168 mm/mm and 820 MPa. The earliest indicated AE event is shown at loading conditions of 0.0103 mm/mm and 590 MPa. This data suggests that the sound camera was able to detect failure precursors at approximately 61 percent ultimate failure strain and 72 percent ultimate failure stress for multi-axial laminates.

5.2 Nondestructive Evaluation Application Parametric Studies

To enhance the accuracy of the diagnostic scheme, numerous post-processing parameters were systematically varied to investigate and assess the wave propagation tracking capabilities of the sound camera in addition to comparing different variations of the basic beamforming algorithm (ultimately, the standard time-domain delay-sum beamforming algorithm presented earlier was used for calculations and preparation of visualizations). These parameters included the temporal and spatial resolutions, and different inspection plate thicknesses. Finally, stress wave visualization and damage detection and localization capabilities were quantified by impact location studies and plates with and without external masses present to simulate damage events. The following sections discuss the results from these studies. For all images shown of the wave propagation tracking, the area presented in the image represents that of the entire inspection plate.

5.2.1 Effects of Temporal Resolution

The temporal resolution was investigated with the goal of achieving a smooth propagation of the transient wave front. In this study, the sound camera MEMS microphones imposed a hardware limitation on the sampling frequency restricting it to 25.6 kHz. This meant the time between individual samples was slightly greater than 39 μs. As discussed later in Section 5.2.3, the wave speed of major flexural wave mode propagation in the 1.02 mm thick plate was approximately 1700 m/s. At this wave speed and the given sampling frequency, the wave front propagated approximately 66.4 mm between each sample or 5.4% of the total plate width. For thicker plates, the wave speed and therefore the propagation distance between samples increased. Given that masses tested to represent psuedo-damage events were on average approximately 60 mm in their smallest dimension, such large propagation distances between samples could lead to mass localization being compromised.

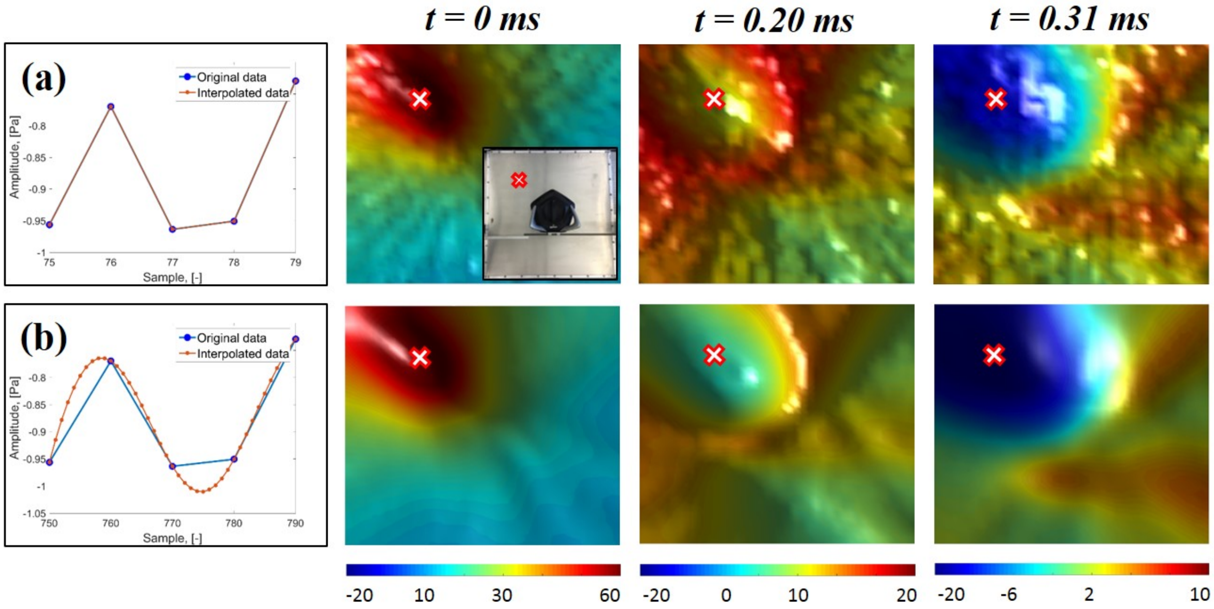

Figure 5.7: Effects of changing temporal resolution using interpolation of results in frequency domain. (a) Raw acoustic signal with no interpolation applied. (b) Raw acoustic signal with upsample factor of 10 applied.

In order to reduce the propagation distance between sequential samples and to improve the resolution of the wave propagation tracking, an interpolation and reconstruction of the raw acoustic signal was performed. Figure 5.7(a) shows a window of the raw signal with no interpolation applied and the drastic amplitude changes pf pressure measured from a microphone between subsequent samples. The beamforming results of the stress wave propagation for the raw signal without interpolation are shown in the three images to the right of the signal. The inset image at $t = 0$ ms in Figure 5.7(a) represents the top left impact induced in the inspection plate. Figure 5.7(b) shows the same raw signal as the one above it, but with a frequency-domain fast fourier transformation interpolation applied to reconstruct the signal. An upsample or resample factor of 10 was chosen for the interpolation in order to decrease the time between samples to 3.9 μs [9]. This meant that the propagation distance between samples was reduced to 6.6 mm and only 0.5% of the total plate width. The drastic effects of the interpolation are seen in the series of images to the right Figure 5.7(b).

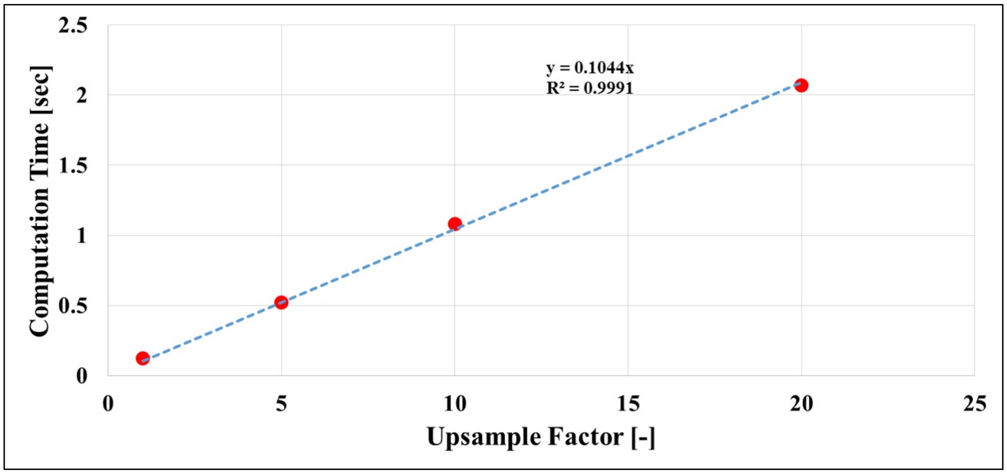

Figure 5.8: Computational time effects of imposing interpolation on raw signal.

Comparing the two sets of images presented in Figure 5.7, we find that both approaches successfully identify the impact location with a reasonably high accuracy (to be further discussed in the later section). However, the results from the raw signal do not show clear boundaries of wave front while the second set of images associated with the interpolated data show the increased definition of the wave front. Additionally, a significant amount of acoustic background noise was removed from the signal which resulted in a refined beamforming image. Looking at $t = 0.20$ ms in Figure 5.7, it is clear that the wave front amplitude is reduced in the reconstructed signal image. The decreased amplitude is due to the more accurate representation of wave front amplitude dissipation resulting from the interpolation of the acoustic signal. This reduces exaggerated pressure amplitude changes observed for the original acoustic signal. From the results, it was determined that an upsample factor of 10 would be suitable for all subsequent simulations. For all temporal resolution studies, the spatial resolution was fixed at approximately 30 mm between adjacent ”pixels.”

While the resolution of the wave propagation was achieved by increasing the upsample factor, a computational penalty was incurred. Based on parametric studies on different upsample factors, the upsample-computational time relationship was approximately linear with an increase in computational time as shown in Figure 5.8. Specifically, for the upsample factor of n, the beamforming computational time is increased $(0.1044 \pm 0.014) \times n$ times compared to the original raw signal. This reduced computational efficiency was deemed an acceptable cost for the increased resolution gained using the reconstructed signal and necessary for identifying and localizing masses. For all subsequent simulations, we used an upsample factor of 10.

5.2.2 Effects of Spatial Resolution

Using the results of the temporal resolution study, the upsample factor was fixed at 10 and the spatial resolution was varied in an attempt to further refine the wave front throughout the propagation time. Figure 5.9 shows the results of the spatial resolution study.

The spatial resolution was systematically halved for each simulation throughout the parametric study. Figure 5.9(a) and corresponding acoustic images show the results for a spatial resolution (ΔX) of 80 mm between pixels. While the impact point in the surface map, marked by the red X, is appropriately localized (compared with the actual impact location as shown in the inset image) the wave front becomes blurry as it begins to propagate into the farfield as seen at times $t = 0.21$ ms and $t = 0.32$ ms. The beamforming images related to Figure 5.9(b) and Figure 5.9(c) show spatial resolutions of 40 mm and 20 mm between pixels,

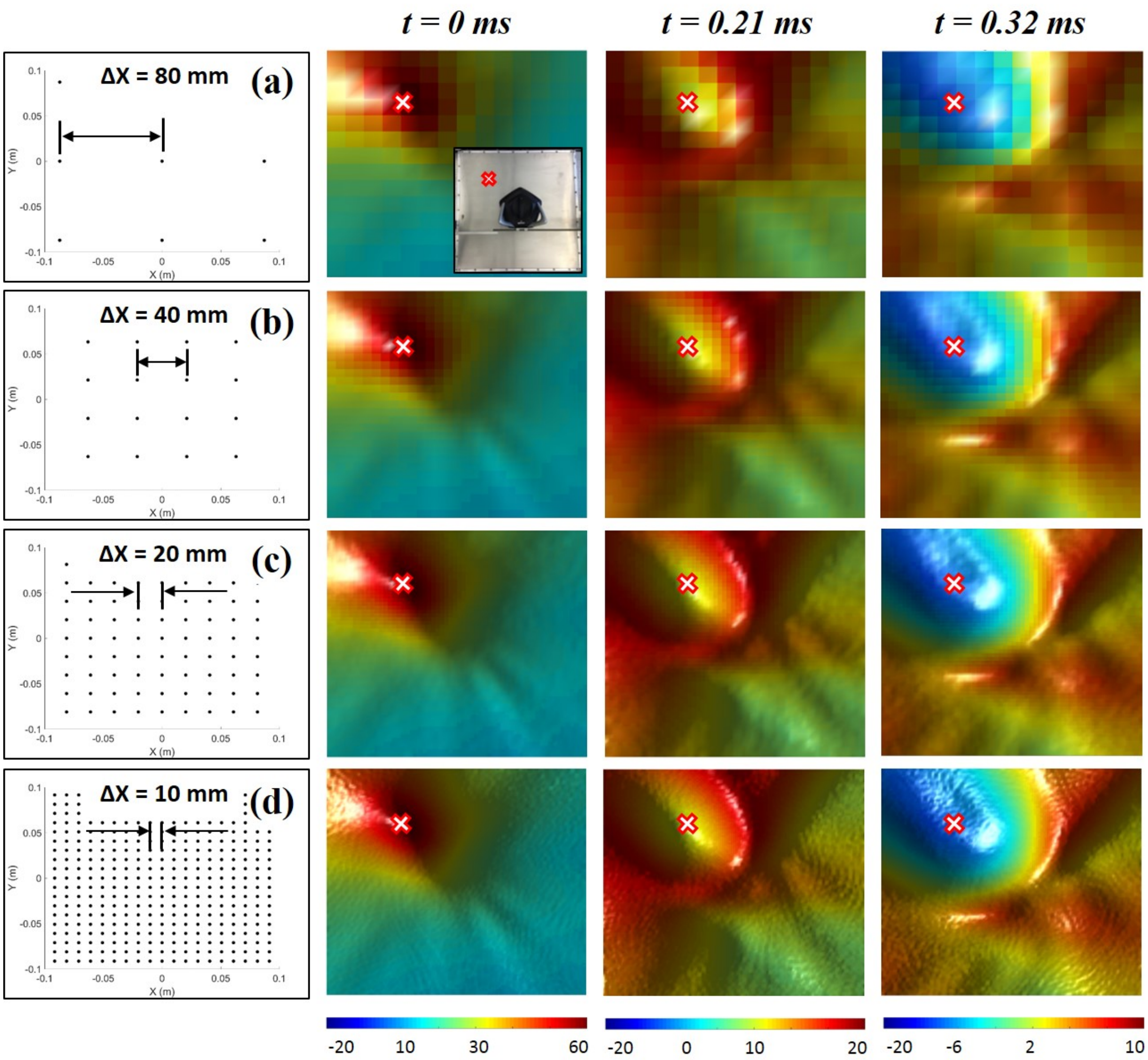

Figure 5.9: Effects of changing spatial resolution by decreasing step size between ”pixels” on virtual inspection plane. Represented are spatial resolutions of (a) 80 mm, (b) 40 mm, (c) 20 mm, and (d) 10 mm.

respectively. Both sets of images again show an accurate impact localization and increased definition of the wave front as the spatial resolution increases. Figure 5.9(d) and associated acoustic images are shown for a ΔX = 10 mm between pixels which is the highest spatial resolution considered in this study. Compared to all previous results, these beamforming images show a very definitive wave front at $t = 0.21$ ms with residual acoustic effects clearly shown in the farfield of the plate. The image at $t = 0.32$ ms for a spatial resolution of 10 mm solidifies that increased spatial resolution can maintain the wave front definition into the farfield of the plate while post-impact saturation behind the wave front clearly emanates from the impact location.

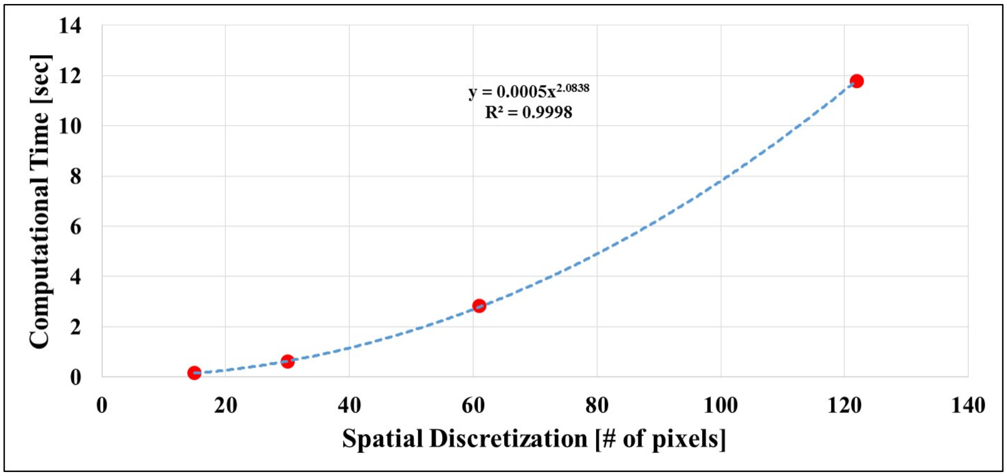

Figure 5.10: Computational time effects of increased spatial resolution imposed on the inspection plate.

While a 10 mm displacement between adjacent pixels may be excessive by highlighting residual acoustic structures, it increases the chance of detecting artificially created damage (to be discussed later) and accurately determining its location. However, for each halving of the spatial resolution, the computational time is increased by a factor of approximately 4.25. Figure 5.10 shows the approximate power-law relationship equal to (2.08 ± 0.042) increase in computational time as the spatial resolution is increased (that is ΔX decreases). The power-law relationship is due to the spatial resolution affecting both dimensions of the inspection plate meaning that the increase in spatial resolution is squared with each iteration. While this leads to a significant increase in computational time, the increase was again considered an acceptable trade-off for the gained wave propagation resolution which would prove necessary for detecting and localizing the masses in subsequent analyses. Following the temporal and spatial resolution studies, a temporal upsample factor of 10 and a spatial resolution of 10 mm were selected for use in all following analyses.

5.2.3 Thickness of Aluminum Plate

In an interest for investigating wave speed effects due to plate thickness, two different aluminum 6061-T6 plates were used as inspection plates for impacts. The beamforming images and calculated wave speeds are presented below.

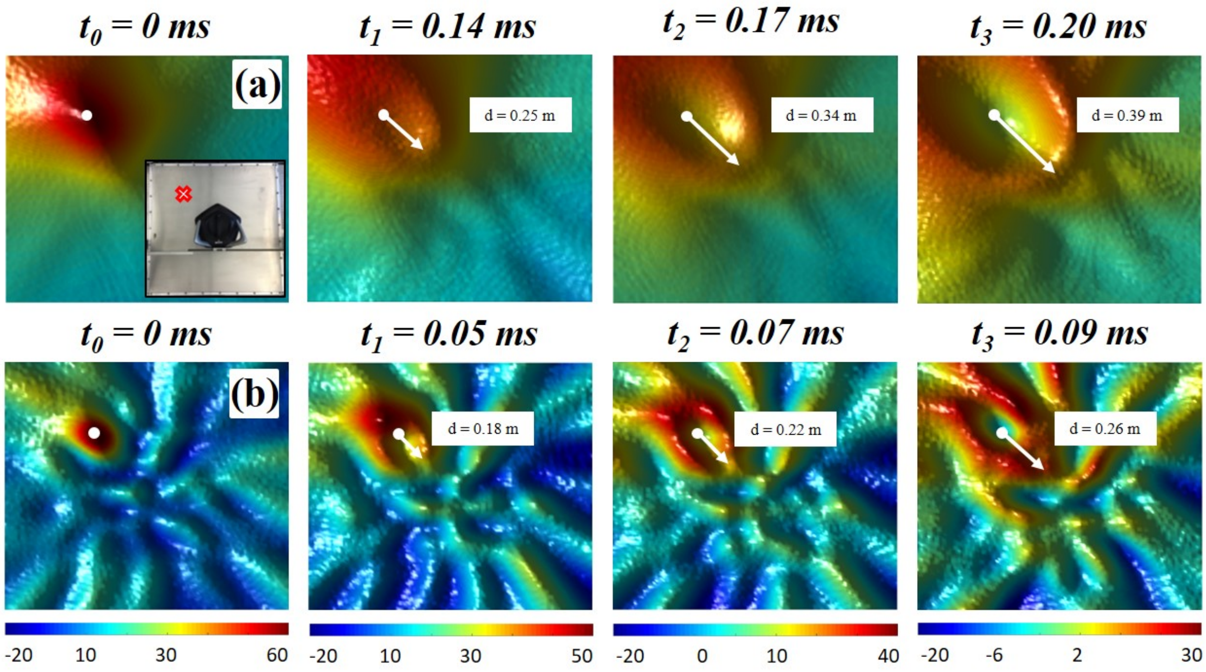

Figure 5.11: Beamforming results for aluminium plates of varying thicknesses. The plates used were aluminum 6061-T6 with thicknesses of (a) 1.02 mm and (b) 6.35 mm.

Figure 5.11 shows the beamforming images for plate thicknesses of 1.02 mm (Fig. 5.11(a), thin plate) and 6.35 mm (Fig. 5.11(b), thick plate). For both plates, the impact location was located in the top left of the plate (shown in the inset image) and is identified by the white dot in all acoustic images. Because of the substantial wave speed difference of nearly 1400 m/s quantified in Table 5.1, beamforming images showing the wave propagation for the thin and thick plate were not correlated in time since the wave had nearly dissipated in the thick plate by the time a definitive wave front was established in the thin plate. This is shown by comparing the propagation images at $t = 0.09$ ms for the thick plate and t = 0.14 ms for the thin plate. In the case of the thick plate, the wave front is beginning to disperse and is losing definition of the primary wave front at this time. However for the thin plate, the wave front is just beginning to form and propagate away from the image location despite being a slightly later image time. Therefore, the wave propagation progression for the thin and thick plate were compared using acoustic images with the same maximum amplitudes. Shown at the bottom of the acoustic images are the color bar which represents the pressure on the plate in units of pascal. This scale needed to be adjusted in time in order to maintain definition of the wave front or else saturation of the image would occur at either the start of the simulation at impact or at the end of the simulation as the wave propagated into the farfield. Therefore, the images were taken as the last acoustic image for each of the plate thicknesses at the maximum pressure shown for the color bar divisions with times denoted for the respective event. As already alluded to, the difference in times alone between similar wave propagation events hints at the difference in wave speed due to the different plate thicknesses. This investigation led to many conclusions about effects of plate thickness in addition to wave speed differences.

The first is that at all instances, the thick plate displayed significantly more residual noise across the farfield of the plate compared to the thin plate. This effect is apparent comparing all images in Figure 5.11. The second is that thick plate enabled a more accurate localization of the impact location indicated by the smaller high amplitude event seen in images at t = 0 ms. The third effect was the difference in wave front dissipation. For the thick plate, the wave front not only propagated faster but also dissipated faster meaning the

Table 5.1: Quantification of wave speed in aluminum 6061-T6 plates of thicknesses equal to 1.02mm and 6.35mm.

Plate Thickness [mm]	Wave Speed: t_0 to t_1 [m/s]	Wave Speed: t_0 to t_2 [m/s]	Wave Speed: t_0 to t_3 [m/s]	Wave Speed: Average [m/s]	Plate Wave Speed [m/s]
1.02	1791.4	1959.2	1936.9	1895.9	1892.5±17.9
6.35	2702.4	2582.4	2943.9	2742.9	2762.6±29.0

wave front amplitude and definition decreased rapidly as it propagated from the point of impact. This led to the wave front dissipating before reaching the farfield as opposed to the thin plate where the wave front is clearly maintained to nearly the other side of the plate from the impact location. The dissipation is seen in the images to the far right where for the thin plate the wave front is clearly visible as the wave front approaches the center of the inspection plate. However for the thick plate, the wave front is already losing definition midway across the plate and soon dissipates entirely. Lastly is the drastic difference in wave speeds observed due to the two plate thicknesses. Table 5.1 gives quantitative wave speed data for the two plate thicknesses.

Wave speeds were calculated between the impact point and each of the three associated acoustic images shown in Figure 5.11 for both plates. The first step for calculating the wave speed was to establish a vector from the impact point to the center of the plate to create a reference direction for distance calculations. For the selected acoustic images/instances, the maximum amplitude point on the wave front located on the established reference vector was selected. The magnitude of the distance vector between the impact point and this point in the wave propagation was calculated and is given in the white boxes in each of the wave propagation images in Figure 5.11. The time between the impact and the selected acoustic image was known and therefore the velocity could easily be determined from the propagation distance divided by the time of propagation to that point. It should be noted that the velocity calculations were very volatile to the calculated distance. Because the propagation times are on the order of microseconds, small discrepancies in distance translated to large velocity differences. Just a few pixels which depended on the spatial resolution could lead to differences of 300+ m/s. The procedure outlined above for calculating the velocity was performed for three individual experiments on both the 1.02 mm and 6.35 mm plates. The average wave speed for each of the experiments was determined from the three intermediate speeds such as discussed above. The average of the average wave speeds was then found in addition to the standard deviation of the individual average wave speeds in order to determine the plate wave speeds given in Table 5.1.

5.3 Application to Nondestructive Evaluations for Damage Detection

Finally, the developed technique and post-processing parameters are evaluated for SHM/NDE purposes with capabilities assessed for detecting different impact locations and defect location simulated with a mass placed in the path of the wave propagation on the inspection plate.

5.3.1 Incident Wave Visualization

Once simulation parameters were determined, tests were performed to characterize detection and localization capabilities of the sound camera. Prior to masses being placed on the plate, it was necessary to determine if different impact locations could be identified since a single impact location in the top left corner of the plate had been used for all previous parametric studies. Additionally, these tests would serve as the first quantitative indication of the detection and localization capabilities. Figure 5.12 shows the qualitative results of the impact location study.

Figure 5.12(a)-(d) represent the relative impact location on the inspection plate. With the center of the inspection plate above which the camera is suspended defined as the origin of the plate, the actual measured impact locations are given in Table 5.2. The wave propagation tracking images for each impact location shown in Figure 5.12(a)-(d) are all correlated in time for each of the different impact locations. For each of the impact locations shown, the

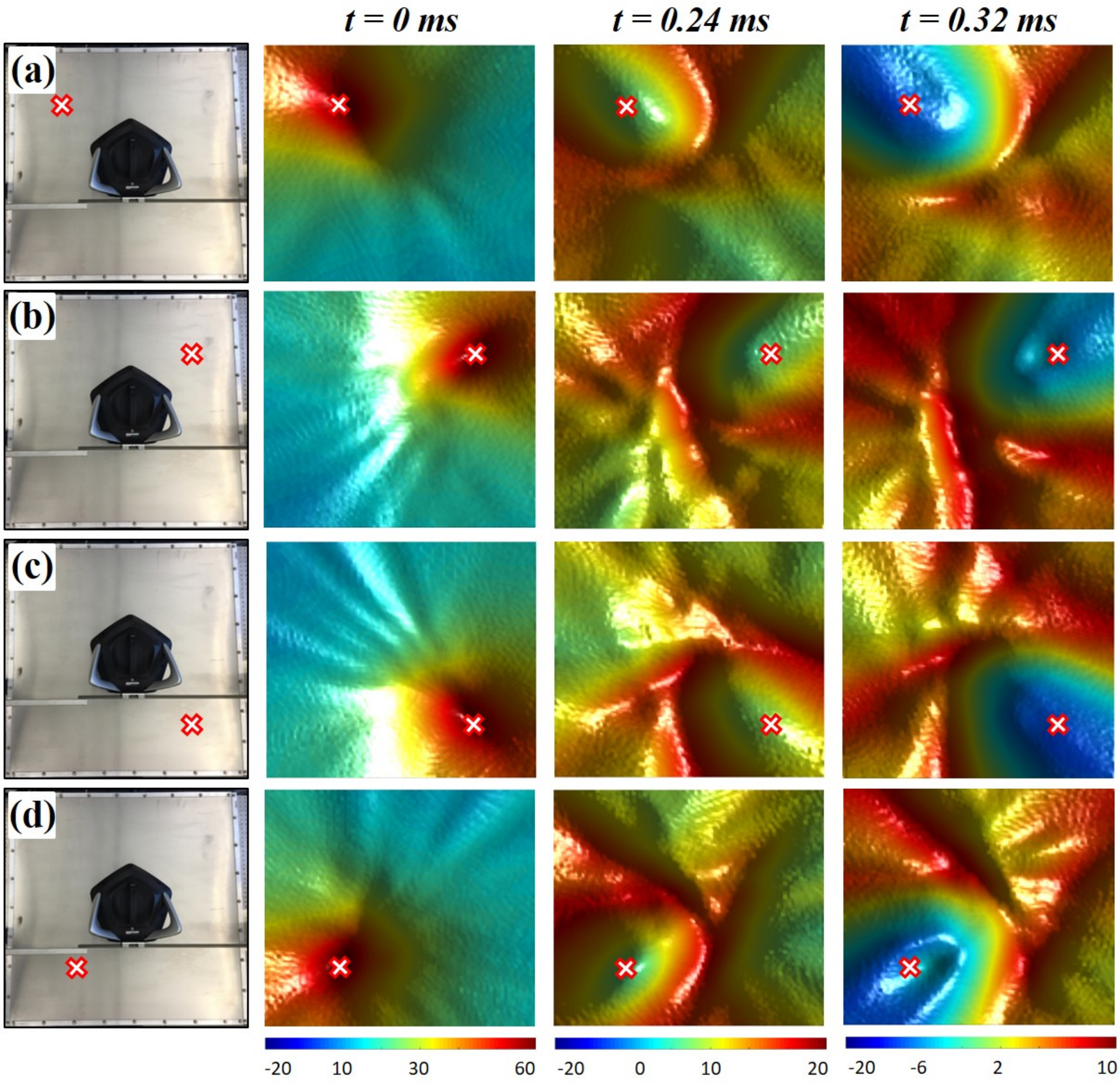

Figure 5.12: Impact locations relative to sound camera and post-processing results showing impact detection capability of the sound camera and beamforming algorithm. Impact locations included (a) top left, (b) top right, (c) bottom right, and (d) bottom left.

images at $t = 0$ ms suggest that the impact location is properly identified and localized using the sound camera and beamforming algorithm. The images shown at $t = 0$ ms were used to identify the point of maximum amplitude at the instant of impact which was defined as the identified impact location. These identified locations are given in Table 5.2.

Table 5.2: Quantification of impact localization.

Impact Location	Actual Position [m,m]	Identified Position [m,m]	Absolute Difference [m]	Normalized Error [Num. Pixels]
Top Left	(-0.3032,0.3048)	(-0.2743,0.3251)	0.0353	3.53
Top Right	(0.3048,0.3064)	(0.3556,0.3150)	0.0515	5.15
Bottom Right	(0.3056,-0.3064)	(0.3150,-0.3251)	0.0209	2.09
Bottom Left	(-0.3040,-0.3056)	(-0.2946,-0.2946)	0.0145	1.45

Looking at actual and identified positions in Table 5.2 (x-position,y-position), it is observed that all impacts were located relatively accurately with regards to identified positions being in the general vicinity of the actual known position of the impact. Using Equation 5.1, the normalized error in terms of number of pixels between the actual and identified impact locations with respect to the spatial discretization was calculated. The calculated errors are given in Table 5.2. Given the ΔX of 10 mm used for this study, the normalized error between the actual and identified impact locations represent differences ranging from 14.5 mm to 51.5 mm as shown in Table 5.2. The largest error was calculated for the top right impact location and found to be 5.15 pixels or approximately 4.22% of the plate width meaning with respect to the total spatial domain in this case, the localization was still relatively accurate. The larger errors could be attributed to not a fine enough spatial resolution which leads to a larger error between the actual and identified locations. Additionally, the larger error values could be due to human error when initiating the impacts on the plate. Impacts were incited by manually tapping the inspection plate at predetermined locations which are noted as the actual impact locations. However, if the impact on the plate were not located at precisely these locations, this would greatly affect the error values as the identified impact location is based off experimental data which assumes the impact is imparted at the actual location.

$$NormalizedError = \frac{\sqrt{\left(X_{actual} - X_{identified}\right)^2 + \left(Y_{actual} - Y_{identified}\right)^2}}{\mathit{\Delta} X} \tag{5.1}$$

The second and third images in the wave propagation sequence show the wave front as it propagates into the farfield of the plate post-impact. For all impact locations, the propagation progression seems relatively similar in terms of wave front amplitude and dissipation. The major difference observed is between the top left impact and the other three impact locations. The top left impact initiates a wave that is very well defined with few acoustic features observed on the plate at t = 0.24 ms other than the wave front. In the other three impact locations, the wave front is well defined as the high amplitude feature on the plate, but it does not retain the definition of the top left impact wave front and other acoustic features seem to stem from the wave front and extend into the farfield. These acoustic features are even more established in the images at t = 0.32 ms despite the wave front contours closely mirroring that of the top left impact. Based on the statistically insignificant error values between actual and identified impact locations and fairly similar wave propagation profiles, this study indicates the sound camera and beamforming algorithm were able to relatively accurately localize different impact locations and track the resultant transient wave across the plate.

5.3.2 With and Without Mass

Once it was established that the sound camera could detect and sufficiently track the transient wave, the impact location was fixed and masses were added to the plate to determine the capability of the sound camera and beamforming algorithm to detect the discontinuities which represented psuedo-damage cases. The impact location used is a top left impact as shown in Figure 5.13(a)-(b). The mass used for this study was a 0.615 kg, 0.0635 m × 0.0635 m stainless steel block. The mass was affixed to the inspection plate using silicon sealant tape that was applied to the entire contact surface of the mass. The use of masses to simulate damage has been used on many occasions to assess the capabilities of different SHM/NDE techniques [21][22]. Figure 5.13(b) shows the mass was place halfway between the impact location and the center of the plate meaning the mass was approximately 0.215 m from the impact location. Figure 5.13 shows the wave propagation results for the inspection without and with the mass present.

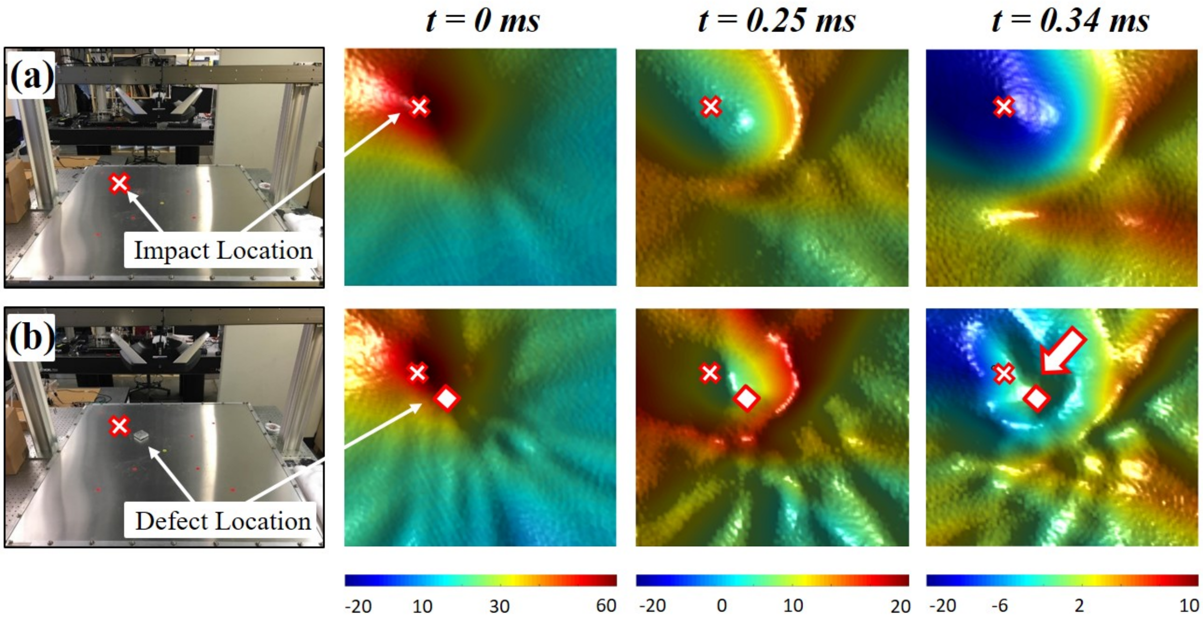

Figure 5.13: (a) Beamforming results for inspection plate with no mass present. (b) Beamforming results for same plate and impact location, but with stainless steel mass affixed to inspection plate.

Figure 5.13 uses a red X and a red square to mark the approximate location of the impact and mass, respectively, on the plate. At $t = 0$ ms, the instant of impact is shown for both the without and with mass cases. These images look very similar between the two cases and there is no indication of a mass being present on the plate. The images at $t = 0.25$ ms show the wave front just after it has propagated past the location of the mass. The first difference is seen in the wave front definition. While the no mass case maintains a smooth and symmetric wave front, the mass case displays a more turbulent wave front with a flatten of the wave front on the far side of the mass relative to the impact point. Additionally, the widespread saturation behind the wave front seen in the no mass case is not seen in the with mass case. In the with mass case, the area behind the wave front maintains a higher acoustic level throughout compared to the no mass case contributing to the less defined wave front. Finally, there is much more acoustic noise in the farfield of the plate for the with mass case compared to the no mass case where the farfield acoustic level is approximately equal to the behind the wave front at $t = 0.25$ ms.

Table 5.3: Quantification of mass detection and localization capability.

Mass Location	Actual Position [m,m]	Identified Position [m,m]	Absolute Difference [m]	Normalized Error [Num. Pixels]
Point 1	(-0.1524,0.1524)	(-0.1219,0.193)	0.0508	5.08

At $t = 0.34$ ms, the most noticeable difference between the no mass and with mass cases is the high amplitude acoustic event present at the location of the mass in the second case. For the no mass case, the wave front is losing amplitude and definition as it propagates and dissipates into the farfield and the area behind the wave front is becoming saturated with low amplitude acoustic levels. However, the backside of the wave front remains very symmetric with respect to the impact location and there is very little excessive acoustic features seen on the plate. In the with mass case, the overall wave front condition appears very similar to that for the no mass case. In terms of dissipation and primary acoustic features, the wave fronts for the two cases display very similar amplitudes and structures at $t = 0.34$ ms. However, despite the similarities the with mass case wave front retains a much less refined wave front at this instance with much more acoustic noise seen in the farfield of the plate. As aforementioned, the most observable and desirable difference is the presence of the acoustic event emanating from the mass location denoted by the red arrow in Figure 5.13 which alludes to the presence of a discontinuity at this location on the inspection plate.

Similar to the impact localization, the maximum amplitude of the acoustic feature near the known location of the mass was used as the identifying location of the mass. This was then compared to the actual location of the mass given in Table 5.3 and using Equation 5.1 the normalized error was calculated between the actual and identified position with respect to the spatial discretization. The calculated error of only 5 spatial pixels represents a fairly high degree of accuracy when identifying the known position of the mass. Given that the mass is 63.5 mm × 63.5 mm, the mass itself is 6.35 pixels × 6.35 pixels. While the exact coordinates of the actual and identified positions do not necessarily correlate, it is likely affected by the acoustic feedback from the mass not emanating from the center of the block. Therefore, if the maximum amplitude were located at one of the points of the mass as it seems to be in Figure 5.13 (corner nearest top edge of plate), this alone would considerably affect the error value. Given the normalized dimensions of the mass, the identified position of the acoustic emission denoting the location of the mass is likely within the bounds of the mass despite the relatively large normalized error.

Chapter 6

CONCLUSIONS AND FUTURE STUDY

> *"Education is the movement from darkness to light."*
>
> Allan Bloom

6.1 Conclusions

This research sought to exploit the capabilities of an air-coupled acoustic array utilizing a beamforming technique for damage detection applications. The research assumed a two prong approach looking at potential applications related to both structural health monitoring and nondestructive evaluation. The research and analysis contained herein strongly support the notion that acoustic emission beamforming can be used for not only detecting the onset of damage events but the ability to accurately isolate the location of these events.

Tensile testing of various composite specimens addressed the non-contact, in-situ SHM capabilities of a sound camera device implementing acoustic beamforming technology. The sound camera was able to accurately detect and locate failure precursors in UD 0° specimens and $[0/\pm45/90]_s$ and $[90/\pm45/0]_s$ laminates. The failure precursors for these laminates tended to be large amplitude and high energy events associated with fiber breakage. It was shown that the sound camera was able to detect when matrix failure occurred in UD 90° specimens. However the indicated location of failure was misrepresented for the majority of the test cases. The misidentified matrix failure location is likely attributed to the lower acoustic feedback resulting from this failure mode. Therefore, further optimization of beamforming array settings and corresponding parameter adjustments are required to detect reduced acoustic feedback characteristics associated with some failure modes.

Visualization of stress wave propagation across an aluminum plate using an air-couple microphone array demonstrated the efficacy of this method as a single-shot NDE technique. The scope of the beamforming method for visualizing stress waves was investigated through various parametric studies that resulted in the establishment of post-processing parameters of upsample factor and spatial resolution for further testing. Subsequent testing revealed the ability of the sound camera to accurately identify various impact locations on the inspection plate. Finally, the beamforming method was used to detect and localize a mass on the inspection plate used to simulate the presence of damage. The sound camera and derived beamforming method were able to relatively accurately locate the position of the mass through the detection of acoustic emission structures indicating the existence of a discontinuity on the inspection plate.

The combination of these studies demonstrate the wide functionality of an acoustic emission beamforming technique for damage detection applications. This research validated the use of an air-coupled sound camera for achieving a non-contact, non-invasive, in-situ monitoring capability. In terms of nondestructive evaluations, the sound camera provides a potential substitute for traditional wave propagation tracking techniques based on laser doppler vibrometry. In contrast to point-by-point measurements across the spatial domain, replicated excitiations required for each measurement, and time correlation of multiple data sets to visualize the wave propagation, the proposed method uses a single-shot measurement to track the wave propagation across the entire spatial domain. In conclusion, this work presents an efficient, effective, and versatile method for detecting and localizing damage events across a wide spectrum of material systems and applications.

6.2 Future Study

While this work provides a good proof of concept for use of acoustic emission beamforming for damage detection, there were numerous areas left unexplored in this research. In terms of structural health monitoring, tensile testing is a very simple and standard test for assessing material systems. However, there exist many other tests to include compression and shear loading and three- and four-point bending tests which are standard tests in the structures industry. The sound camera could easily be used during these tests to determine its ability for monitoring materials under various loading and damage scenarios. One of the most intriguing studies would involve the use and comparison of digital image correlation or ultrasonic testing methods. During loading of the specimen, the sound camera could be used to monitor the specimen for evidence of an acoustic emission signifying the onset of a damage event. These other methods could then be used to determine the exact type of damage such as cracks, delaminations, etc. By knowing the type of damage and the acoustic event detected by the camera, it may be possible to quantify the acoustic emissions in some manner to determine the type of damage mode purely from the acoustic feedback received. This could easily be expanded to using the acoustic emissions received for tracking the exact location and propagation of the damage through the specimen. Tracking the damage events was briefly explored but was not brought to fruition in this work.

For detecting damage on a plate, there exist many ways to expand this study to further exploit and characterize the capabilities of the sound camera and the beamforming method. The first study should include altering the location of the mass on the plate. The distance between the impact and mass locations should be systematically increased to determine the true spatial domain which this method can monitor at once. After the feasible detection distance has been quantified, the mass should be moved to various locations within this radius across the plate to investigate the interactions between the mass and the boundary of the plate and whether the mass is still able to be detected when located near the boundary. Next, the minimum size of detectable mass should be determined. This study should be two-fold including masses of the same size but different mass, and masses of differing size but the same mass. I believe this will give a more holistic view of the damage detection capabilities of the acoustic emission approach. Finally, multiple masses should be included in a single test to determine if numerous damage events can be detected in a single-shot manner. By exploring these questions and others, the overall capabilities and advantages presented by the sound camera and acoustic emission beamforming technique can be greatly bolstered.

Regardless of the application, the beamforming algorithm can be greatly refined and manipulated to assist in achieving more accurate post-processing results. Additional hardware limitations including the microphones used should be explored to investigate the full extent of this method. Despite the vast array of applications still unexplored, acoustic emission beamforming is a promising method for detection and monitoring capabilities necessary for ensuring safe and reliable utilization of next-generation materials and structures.

BIBLIOGRAPHY

[1] Giurgiutiu V 2015 *Structural Health Monitoring of Aerospace Composites* (Academic Press).

[2] Johnson S B 2011 *System Health Management: With Aerospace Applications* (John Wiley & Sons, Ltd)

[3] Wang M L, Lynch J P, Sohn H 2014 *Sensor Technologies for Civil Infrastructures: Applications in Structural Health Monitoring* (Woodhead Publishing)

[4] The American Society for Nondestructive Testing, *Introduction to Nondestructive Testing*, Web, 2015.

[5] B. Boro Djordjevic, *Nondestructive Test Technology for the Composites*, The 10th International Conference of the Slovenian Society for Non-Destructive Testing, pages 259-265, Materials and Sensors Technologies Inc., 2015.

[6] NDT Resource Center, *Introduction to Acoustic Emission Testing*, National Science Foundation - Advanced Technological Education.

[7] P Rizzo, F Lanza di Scalea, *Acoustic emission monitoring of carbon-fiber-reinforced-polymer bridge stay cables in large-scale testing*, Experimental Mechanics, 41:3, 282, 2001.

[8] Charles Hellier, *Handbook of Nondestructive Evaluation: Chapter 10 - Acoustic Emission Testing*, McGraw Hill, 2nd Edition, 2012.

[9] Gregory C. McLaskey, Steven D. Glaser, Christian U. Grosse, *Acoustic Emission*

Beamforming for Enhanced Damage Detection, Sensors and Smart Structures Technologies for Civil, Mechanical, and Aerospace Systems, Proc. of SPIE Vol. 6932(39):1-9, 2008.

[10] Christian U. Grosse, *Acoustic Emission Localization Methods for Large Structures Based on Beamforming and Array Techniques*, Non-Destructive Testing in Civil Engineering, Nantes, France, 2009.

[11] Steven E. Olson, Martin P. DeSimio, Mark M. Derriso, *Beam Forming of Lamb Waves for Structural Health Monitoring*, The American Society of Mechanical Engineers, Journal of Vibration and Acoustics, Vol. 129(6):730-738, December 2007.

[12] Sanjay Sengupt, Aloke Kumar Datta, Pijush Topdar, *Structural Damage Localisation by Acoustic Emission Technique: A State of the Art Review*, Latin American Journal of Solids and Structures, Vol. 12(8):1565-1582, 2015.

[13] M. Wevers, *Listening to the Sound of Materials: Acoustic Emission for the Analysis of Material Behavior*, NDT & E International, 30:99-106, 1997.

[14] NDT Resource Center, *NDT Method Summary*, National Science Foundation - Advanced Technological Education.

[15] NDT Resource Center, *Introduction to Acoustic Emission Testing*, National Science Foundation - Advanced Technological Education.

[16] Robert P. Dougherty, *Functional Beamforming*, 5th Berlin Beamforming Conference, Berlin, Germany, 2014.

[17] Ronald Mucci, *A Comparison of Efficient Beamforming Algorithms*, IEEE Transactions on Acoustics Speech and Signal Processing, 32(3):548-558, June 1984.

[18] Joe C Chen, Kung Yao, Ralph E Hudson, *Acoustic Source Localization and Beamforming: Theory and Practice*, EURASIP Journal on Applied Signal Processing, 4:359-370, 2003.

[19] Ulf Michel, *History of Acoustic Beamforming*, Berlin Beamforming Conference (BeBeC), BeBeC-2006, Berlin, Germany, November 2006.

[20] SM Instruments, *SeeSV-S205 Portable Sound Camera Product Overview and Specifications*, SM Instruments Inc, Daejeon, Korea, August 2014.

[21] A. Kody, X. Li, B. Moaveni, *Identification of Physically Simulated Damage on a Footbridge Based on Ambient Vibration Data*, American Society of Civil Engineers Structures Congress 2013, 352-362, 2013.

[22] Douglas Adams, *Health Monitoring of Structural Materials and Components: Methods with Applications*, John Wiley & Sons Ltd., West Sussex, England, 2007.

[23] Faeez A. Masurkar, Nitesh P. Yelve, *Locating a Damage in and Aluminum Plate Using Lamb Waves*, NDE 2015, Hyderabad, November 2015.

[24] Joshua C. Rivey, Gil-Yong Lee, Jinkyu Yang, et. al, *Acoustic Emission Beamforming for Detecting and Localizing Damage in Composite Materials*, 57th AIAA/ASCE/AHS/ASC Structures, Structural Dynamics, and Materials Conference, AIAA SciTech, AIAA 2016-0664.

[25] Joshua C. Rivey, Gil-Yong Lee, Jinkyu Yang, et. al, *Visualization of Stress Wave Propagation via Air-Coupled Acoustic Emission Sensors*, Society for Experimental Mechanics, Inc., 2016 SEM 13th International Congress & Exposition on Experimental and Applied Mechanics, 2016.

[26] Joshua C. Rivey, Gil-Yong Lee, Jinkyu Yang, et. al, *Visualization of Stress Wave Propagation via Air-Coupled Acoustic Emission Sensors*, Society for Experimental Mechanics, Inc., Pending submission to Smart Materials and Structures, 2016.

Appendix A

STRUCTURAL HEALTH MONITORING POST-PROCESSING

A.1 Load Data

```
videoobj = VideoReader('0-45-90-3_20150729_135955_[0.0s-113.7s]...
           _Average[exp. 3]_Threshold[40.0]_Range[1.0].avi');
vidFrames = read(videoobj);
numFrames = get(videoobj, 'numberOfFrames');
filename = 'Specimen_RawData_60.csv';
Data = xlsread(filename);
%Video extensomer
Data(1:13,:) = [];
xvalues = Data(:,5);
yvalues = Data(:,4);
```

A.2 Initialize Video File and Time-Correlate Data

```
kstart = (numFrames-2.5*length(Data));
kstart = floor(kstart);
writerObj = VideoWriter('DamageProp_0_45_90_analysis.avi');
writerObj.FrameRate = 10;
open(writerObj);
for k = kstart:numFrames
    mov(k).cdata = vidFrames(:,:,:,k);
    mov(k).colormap = [];
```

A.3 Refine Inspection Window and Plot Recorded Acoustic Emission Events and Close Video File

```
initialx = 280;
    finalx = 360;
    initialy = 100;
    finaly = 400;
    [a,b]=find(vidFrames(initialy:finaly,initialx:finalx,1,k) ≥ 220);
    if numel(a) > 80    %a = 80 for video extensomer, 60 without
        [c,d]=find(vidFrames(initialy:finaly,initialx:finalx,3,k) ≥ 220);
        if numel(c) > 65    %c = 65 for video extensomer, 50 without
            fig = figure('position',[1 1 1919 1079]);
            axes('Position',[0.1, 0.15, 0.8, 0.8]);
            plot(xvalues(1:round(((k-kstart))/2.5),1),...
                 yvalues(1:round(((k-kstart))/2.5),1),...
                'Marker','o',...
                'MarkerSize',4,...
                'MarkerEdgeColor','b',...
                'MarkerFaceColor','b');
            xlim([0 max(xvalues+0.001)]);
            ylim([0 max(yvalues+5)]);
            set(gca,'FontSize',16);
            xlab = get(gca,'xlabel');
            xlabel('\epsilon, [mm/mm]');
            set(xlab,'Fontsize',24);
            ylab = get(gca,'ylabel');
            ylabel('\sigma, [MPa]');
            set(ylab,'Fontsize',24);
            grid on;
            hold on;
            xdamage(event,1) = xvalues(round(((k-kstart))/2.5),1);
            ydamage(event,1) = yvalues(round(((k-kstart))/2.5),1);
```

```
            scatter(xdamage(:,1),ydamage(:,1),50,...
                'MarkerEdgeColor','k',...
                'MarkerFaceColor','r',...
                'LineWidth',3);
            hold on;
            event = event+1;
            axes('Position',[0.125, 0.625, 0.3, 0.3]);
            imshow(mov(k).cdata);
            filename = ['Images\0-45-90_analysis' num2str(event)];
            print(filename,'-dpng');
            F = getframe(fig);
            writeVideo(writerObj,F);
        end
    end
end
close(writerObj);
```

Appendix B

NONDESTRUCTIVE EVALUATION POST-PROCESSING

B.1 Load Data, Refine Sample Window, and Declare Sampling Parameters

```
%Load Data
data = textread('M1_Point3.txt');
%Plot Data for Entire Capture Time
figure;
plot(data)
set(gca,'FontSize',12)
xlabel('Sample, [-]','FontSize',18);
ylabel('Amplitude, [Pa]','FontSize',18);
%Declaring Selection of Samples from Entire Data Set to Analyze
[Max_Amp,I_Amp] = max(data(:));
[I_row,I_column] = ind2sub(size(data),I_Amp);
Start_Sample = I_row-10; %Original = 50
End_Sample = I_row+200;
Sample_Window = Start_Sample:End_Sample;
Analysis_Data = data(Sample_Window,:);
%Plot Data for Analysis Window
figure;
plot(Analysis_Data)
set(gca,'FontSize',12)
xlabel('Sample, [-]','FontSize',18);
ylabel('Amplitude, [Pa]','FontSize',18);
%Sampling Frequency of Phased Array = 25.6 kHz
Sample_Freq = 25600;
%Number of Microphone Channels on Phased Array
```

```
Num_Ch = 30;
%Speed of Sound in Air (meters/sec)
Speed_Sound_air = 340;
```

B.2 Define Area and Discretization of the Inspection Plate

```
L = 1.2192; %meter
n = 122; %number of pixels
x = linspace(-L/2,L/2,n);
y = linspace(-L/2,L/2,n);
[X,Y] = meshgrid(x,y);
Z = zeros(n,n);
```

B.3 Define Microphone Positions with Respect to the Inspection Plate

```
Height_of_Array = 520.7*10^-3; %meters
%Microphone Positions Provided by SMI
X1 = [-0 0.019 0.049 0.083 0.118 0.15];
Y1 = [0.047 0.08 0.1 0.105 0.0955 0.064];
X2 = [0.0445 0.0815 0.11 0.126 0.127 0.107];
Y2 = [0.0145 0.0065 -0.0155 -0.0465 -0.083 -0.1235];
X3 = [0.0275 0.0315 0.0195 -0.0055 -0.039 -0.084];
Y3 = [-0.038 -0.0755 -0.11 -0.134 -0.1465 -0.14];
X4 = [-0.0275 -0.062 -0.098 -0.129 -0.151 -0.159];
Y4 = [-0.038 -0.053 -0.052 -0.0365 -0.0085 0.037];
X5 = [-0.0445 -0.07 -0.08 -0.074 -0.0545 -0.014];
Y5 = [0.0145 0.043 0.077 0.112 0.1415 0.163];
XX = [X1 X2 X3 X4 X5];
YY = [Y1 Y2 Y3 Y4 Y5];
ZZ = Height_of_Array*ones(1,Num_Ch);
```

```
%Microphone Position Vector
Mic_Pos = [XX;YY;ZZ];
%Plot Location of All Microphones in the Array
figure;
plot(X1,Y1,'.k','MarkerSize',28,'MarkerEdgeColor','k','MarkerFaceColor','k')
hold on;
plot(X2,Y2,'.b','MarkerSize',28,'MarkerEdgeColor','b','MarkerFaceColor','b')
plot(X3,Y3,'.r','MarkerSize',28,'MarkerEdgeColor','r','MarkerFaceColor','r')
plot(X4,Y4,'.m','MarkerSize',28,'MarkerEdgeColor','m','MarkerFaceColor','m')
plot(X5,Y5,'.g','MarkerSize',28,'MarkerEdgeColor','g','MarkerFaceColor','g')
str = {'1','2','3','4','5','6','7','8','9','10','11','12','13','14','15',...
    '16','17','18','19','20','21','22','23','24','25','26','27','28',...
    '29','30'};
text(XX+0.007,YY,str,'fontsize',14,'fontweight','b');
hold on;
scatter(0,0,200,'o','MarkerEdgeColor','k','MarkerFaceColor',[.5 .5 .5],...
        'LineWidth',2);
xlabel('X (m)','fontsize',14,'fontweight','b');
ylabel('Y (m)','fontsize',14,'fontweight','b');
set(gca,'FontSize',14)
xlim([-0.2,0.2]);
ylim([-0.2,0.2]);
%Save Microphone Position Figure as .png
filename = ['Images\MicPos'];
print(filename,'-dpng');
```

B.4 *Calculate Delays Across Spatial Domain to Microphone Array*

```
%X-Position
for i = 1:length(X)
    %Y-Position
    for j = 1:length(Y)
```

```
        %Microphone Channel
        for k = 1:Num_Ch
            %Magnitude of Vector from Point(i,j) to Reference Point on
            %Microphone Array (Center of Array)
            X_Ref(i,j,k) = sqrt(X(i,j)^2+Y(i,j)^2+(Height_of_Array)^2);
            %Magnitude of Vector from Point(i,j) to Microphone 'k' on
            %Microphone Array
            X_Ch(i,j,k) = sqrt((X(i,j)-XX(k))^2+(Y(i,j)-YY(k))^2+(ZZ(k))^2);
            %Calculate Delay of Signal from Point(i,j) to Microphone 'k' in
            %Seconds
            Delay_sec(i,j,k) = (X_Ch(i,j,k)-X_Ref(i,j,k))/Speed_Sound_air;
            %Calculate Delay of Signal from Point(i,j) to Microphone 'k' in
            %# of Samples
            Delay_Samples(i,j,k) = Delay_sec(i,j,k)*Sample_Freq;
        end
    end
end
```

B.5 Apply Zeropadding to Refined Sample Window

```
%Finding Maximum Delay of Samples for Zeropadding of Samples
Max_Delay = max(Delay_Samples(:));
Max_Delay_Int = ceil(Max_Delay);
Analysis_Data_Zeropad = padarray(Analysis_Data,Max_Delay_Int);
Zeropad_Start = Start_Sample-Max_Delay_Int;
Zeropad_End = End_Sample+Max_Delay_Int;
Zeropad_Window = Zeropad_Start:Zeropad_End;
figure;
plot(Zeropad_Window,Analysis_Data_Zeropad)
set(gca,'FontSize',12)
xlabel('Sample, [-]','FontSize',18);
ylabel('Amplitude, [Pa]','FontSize',18);
```

B.6 Apply Fast Fourier Interpolation to Refined Sample Window

```
y = Analysis_Data_Zeropad;
N = size(Analysis_Data_Zeropad,1);
%Define the upsample factor
Upsample_Factor = 10;
M = N*Upsample_Factor;
x = 0:Upsample_Factor:Upsample_Factor*N-1;
xi = 0:M-1;
Analysis_Data_Interp = interpft(y,M);
figure
plot(x,y(:,1),'-o','LineWidth',3,'MarkerSize',10,'MarkerEdgeColor','b',...
'MarkerFaceColor','b')
hold on;
plot(xi,Analysis_Data_Interp(:,1),'-*','LineWidth',2,'MarkerSize',7)
set(gca,'FontSize',18)
xlabel('Sample, [-]','FontSize',22);
ylabel('Amplitude, [Pa]','FontSize',22);
Legend = legend('Original data','Interpolated data');
set(Legend,'FontSize',22);
```

B.7 Perform Simple Time-Domain Delay-Sum Beamforming

```
t_start = Max_Delay_Int*Upsample_Factor;
t_end = t_start+30*Upsample_Factor;
for t = t_start:t_end
    %X-Position
    for i = 1:length(X)
```

```
        %Y-Position
        for j = 1:length(Y)
            %Microphone Channel
            for k = 1:Num_Ch
            Signal(k) = Analysis_Data_Interp(t+...
                        round(Delay_Samples(i,j,k)*Upsample_Factor),k);
            end
            Beamforming(i,j,t) = sum(Signal(:));
        end
    end
end
```

B.8 Plot the Beamforming Image on Inspection Plate

```
vid = VideoWriter('Beamforming_M1_Point3.avi');
vid.FrameRate = 5;
open(vid);
for p = t_start:t_end
    figure%('Visible','off');
    surf(X,Y,Beamforming(:,:,p))
    hold on;
    camlight left;
    lighting phong;
    shading interp
    colormap('jet')
    az = 0;
    el = 90;
    view(az,el)
    colorbar;
    grid off;
    if p > P_max
    if max(max(Beamforming(:,:,p))) < 0
```

```
c_low = -20;
c_high = 0;
caxis([c_low c_high]);
elseif max(max(Beamforming(:,:,p))) < 10
c_low = -20;
c_high = 10;
caxis([c_low c_high]);
elseif max(max(Beamforming(:,:,p))) < 20
c_low = -20;
c_high = 20;
caxis([c_low c_high]);
elseif max(max(Beamforming(:,:,p))) < 30
c_low = -20;
c_high = 30;
caxis([c_low c_high]);
elseif max(max(Beamforming(:,:,p))) < 40
c_low = -20;
c_high = 40;
caxis([c_low c_high]);
elseif max(max(Beamforming(:,:,p))) < 50
c_low = -20;
c_high = 50;
caxis([c_low c_high]);
else
c_low = -20;
c_high = 60;
caxis([c_low c_high]);
end
else
c_low = -20;
c_high = 60;
caxis([c_low c_high]);
end
```

```
    xlim([-L/2 L/2]);
    ylim([-L/2 L/2]);
    %Plot the Impact Point (Top Left)
    Impact_X = -0.3032;
    Impact_Y = 0.3048;
    scatter3(Impact_X,Impact_Y,max(max(Beamforming(:,:,p)))+1,...
    36,'MarkerEdgeColor','k','MarkerFaceColor','white',...
    'LineWidth',2)
    hold on;
     %Plot the Damage Point (Point 1)
     Damage_X = -0.1524;
     Damage_Y = 0.1524;
%     %Plot the Damage Point (Point 2)
%     Damage_X = 0.1524;
%     Damage_Y = 0.1508;
%    %Plot the Damage Point (Point 3)
%    Damage_X = 0.1627;
%    Damage_Y = -0.1524;
%     %Plot the Damage Point (Point 4)
%     Damage_X = -0.1524;
%     Damage_Y = -0.1524;
    scatter3(Damage_X,Damage_Y,max(max(Beamforming(:,:,p)))+1,...
    70,'MarkerEdgeColor','k','MarkerFaceColor','white',...
    'LineWidth',2)
    hold on;
    xlabel('X (m)','fontsize',14,'fontweight','b')
    ylabel('Y (m)','fontsize',14,'fontweight','b')
    zlabel('Pressure (Pa)')
    %save as png
    titlename=['Beamforming output at t = ' num2str(p/...
              (Sample_Freq*Upsample_Factor)*1000) 'msec'];
    title(titlename,'fontsize',14,'fontweight','b')
    filename = ['M1_Point3\Beamforming' num2str(p)];
```

```
    print(filename,'-dpng');
    % Create AVI file.
    drawnow;
    set(gcf, 'Renderer', 'painters')
    M = getframe(gcf);
    writeVideo(vid,M);
end
```

Appendix C

MICROPHONE DELAYS

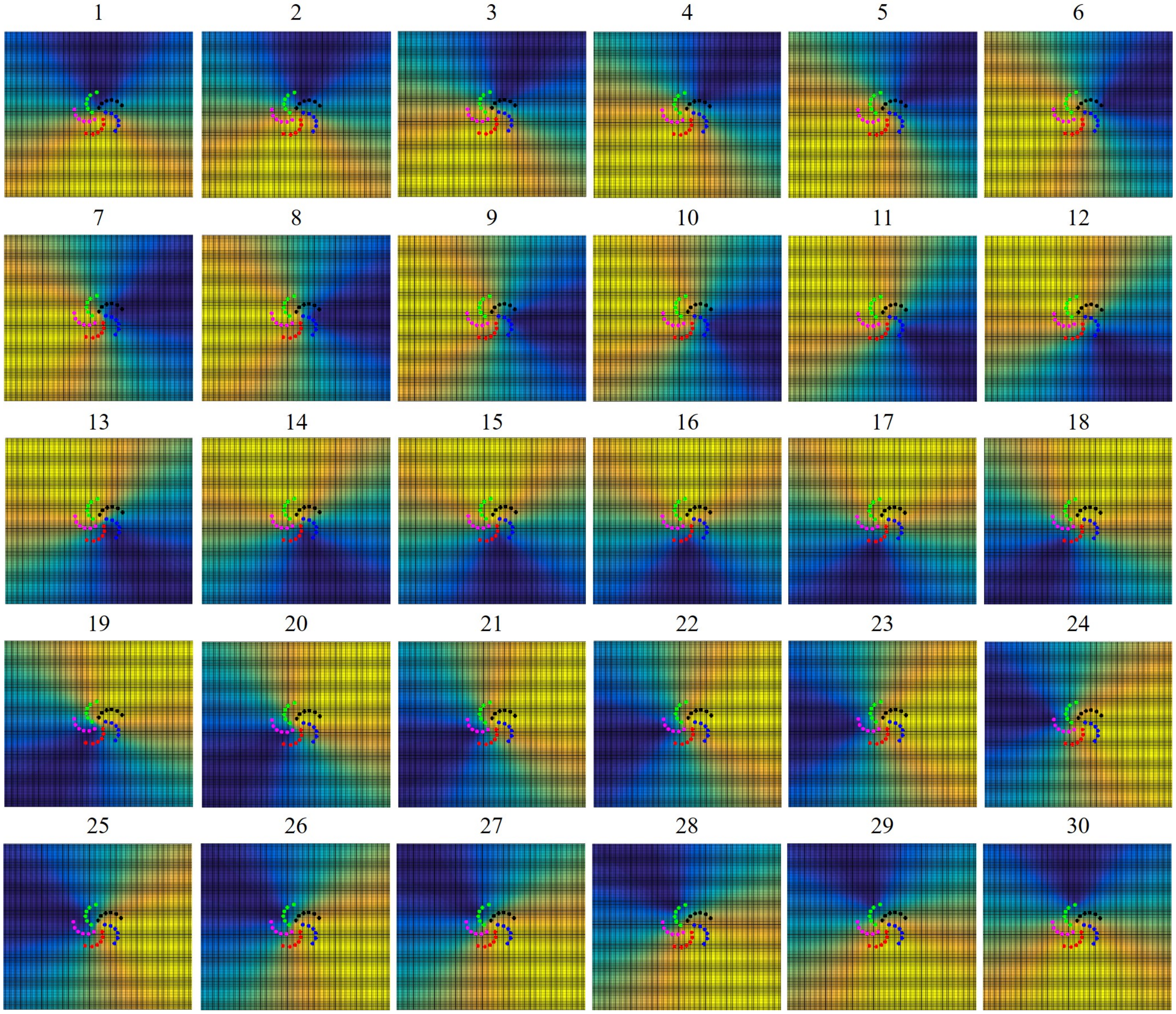

Figure C.1: Time delay in seconds from microphone 7 to substrate for array height from substrate of 20 milimeters.